UCLA
UCLA Electronic Theses and Dissertations

Title
Quantification of live cell mass dynamics for drug efficacy assessment and growth studies

Permalink
https://escholarship.org/uc/item/4cn7v8p9

Author
Chun, Jennifer

Publication Date
2014

Supplemental Material
https://escholarship.org/uc/item/4cn7v8p9#supplemental

Peer reviewed|Thesis/dissertation

eScholarship.org Powered by the California Digital Library
University of California

UNIVERSITY OF CALIFORNIA

Los Angeles

Quantification of live cell mass dynamics for drug efficacy assessment and growth studies

A dissertation submitted in partial satisfaction of the

requirements for the degree Doctor of Philosophy

in Biomedical Engineering

by

Jennifer Kathleen Chun

2014

ABSTRACT OF THE DISSERTATION

Quantification of live cell mass dynamics
for drug efficacy assessment and growth studies

By

Jennifer Kathleen Chun

Doctor of Philosophy in Biomedical Engineering

University of California, Los Angeles, 2014

Professor Michael Alan Teitell, Chair

Direct measurement of cell mass and growth can be difficult with traditional techniques, leaving unanswered questions about how exactly cells grow and divide and how cell mass responds to changes in state or therapeutic treatment. A challenge encountered by other developing mass measurement techniques is accommodating the breadth in the modes of growth of various cell types. This dissertation introduces and develops live cell interferometry (LCI) for the optical tracking and rapid mass profiling of live cells with varying growth types. Mass quantification is demonstrated with picogram resolution on both adherent and non adherent cells as well as single cells and colony-forming cells. The flexibility and speed of the LCI is applied to assess the sensitivity of four human breast cancer lines (BT-474, MDA-MB-231, SK-BR-3, MCF-7) to the HER2-directed monoclonal antibody trastuzumab (Herceptin) and to the growth dynamics of human pluripotent stem cells (HSF1) differentiating under retinoic acid treatment. With the LCI, detecting the sensitivity of the breast cancer lines to trastuzumab is 20 times faster than traditional proliferation assays, an important advancement towards individualized cancer

treatment where patient samples are fragile. Dense clusters of stem cells also pose no barrier and intracolony motion is quantified in addition to overall colony growth.

The dissertation of Jennifer Kathleen Chun is approved.

Dino Di Carlo

Pei-Yu Chiou

Chih-Ming Ho

Kathleen M. Sakamoto

Michael Alan Teitell, Committee Chair

University of California, Los Angeles

2014

DEDICATION

For Mom, Dad, and Joey

TABLE OF CONTENTS

Abstract of Dissertation ii

Committee iv

Dedication v

Table of Contents vi

Acknowledgements vii

Vita ix

Chapter 1

Introduction 1

References……. 6

Chapter 2

Rapid, massively parallel single-cell drug response measurements via live cell interferometry 8

References……. 38

Chapter 3

Rapidly quantifying drug sensitivity of dispersed and clumped breast cancer cells by mass profiling 41

References……. 52

Chapter 4

Quantification of biomass and cell motion in human pluripotent stem cell colonies 53

References……. 91

Chapter 5

Conclusion 94

ACKNOWLEDGMENTS

Chapter two is a version of [Reed J, Chun J, Zangle TA, Kalim S, Hong JS, Pefley SE, Zheng X, Gimzewski JK, Teitell MA. Rapid, massively parallel single-cell drug response measurements via live cell interferometry. Biophys J. 2011 Sep 7;101(5):1025-31. doi: 10.1016/j.bpj.2011.07.022.]. J.R., S.K., J.K.G., M.A.T. designed the experiments. J.R., J.C., T.A.Z., and J.S.H. performed experiments. J.R., J.C., T.A.Z., S.E.P., X.Z., M.A.T. analyzed the data. J.R., J.C., T.A.Z., and M.A.T. wrote the manuscript. This project is supported by an UC Discovery/Abraxis Bioscience Biotechnology Award (Bio07-10663), by the NIH Roadmap for Medical Research Nanomedicine Initiative (PN2EY018228) and by NIGMS (R21GM074509). We thank K. Niazi and S. Rabizadeh (Abraxis and CNSI, UCLA) for helpful discussions.

Chapter three is a version of [Chun J, Zangle TA, Kolarova T, Finn RS, Teitell MA, Reed J. Rapidly quantifying drug sensitivity of dispersed and clumped breast cancer cells by mass profiling. Analyst. 2012 Dec 7;137(23):5495-8. doi: 10.1039/c2an36058f.] - Reproduced by permission of The Royal Society of Chemistry. J.C., T.K., R.S.F., and M.A.T. designed the experiments. J.C. performed experiments. J.C., T.A.Z., M.A.T., and J.R. analyzed the data. J.C., M.A.T., and J.R wrote the manuscript. This project is supported by the Whitcome Training Program (to J.C.), NIH training grants (T32CA009120 and CA157940 to T.A.Z.), a UC Discovery Biotechnology Award (Bio07-10663 to M.A.T.), the NIH Roadmap for Medical Research Nanomedicine Initiative (PN2EY018228 to M.A.T.) and by NIGMS (R01GM094388 to J.R.). We thank K. Niazi and S. Rabizadeh (NantWorks and CNSI, UCLA) for helpful discussions.

Chapter four is a version of [Zangle TA, Chun J, Zhang J, Reed J, Teitell MA. Quantification of biomass and cell motion in human pluripotent stem cell colonies. Biophys J. 2013 Aug 6;105(3):593-601. doi: 10.1016/j.bpj.2013.06.041.]. T.A.Z., J.R., and M.A.T. designed the experiments and wrote the manuscript. T.A.Z., J.C., and J.Z. performed experiments. T.A.Z, J.C, J.R., and M.A.T. analyzed the data. This study is supported by a UC Discovery Biotechnology Award (Bio07-10663), a California Institute for Regenerative Medicine Basic Biology 1 Award (CIRM RB1-01397), the Broad Stem Cell Research Center at UCLA Innovator Award, by the NIH Roadmap for Medical Research Nanomedicine Initiative (PN2EY018228), by NIH/NIGMS grants (T32CA009120, T32CA009056, P01GM081621, K25CA157940, and R01GM094388), and partially supported by a Translational Acceleration Grant from the Caltech-UCLA Joint Center for Translational Medicine (www.jctm.caltech.edu). We thank K. Niazi and S. Rabizadeh (NantWorks and CNSI, UCLA) for helpful discussions.

I'd like to thank my committee, the Teitell lab, the Nantworks/CNSI lab, and BME IDP for their support and guidance. I'm also grateful to the friends that have stayed with me through thick and thin and my family, who I couldn't do without.

VITA

Education

University of California, Los Angeles: Los Angeles, CA
Henry Samueli School of Engineering and Applied Sciences
Biomedical Engineering Interdepartmental Program
Molecular and Cellular Bioengineering
Master of Science, 2010

University of California, San Diego: La Jolla, CA
Jacobs School of Engineering
Bioengineering: Biotechnology, Language Studies: Chinese
Bachelor of Science, 2009

Publications and Proceedings

Zangle TA, **Chun J**, Zhang J, Reed J, Teitell MA. Quantification of biomass and cell motion in human pluripotent stem cell colonies. Biophys J. 2013 Aug 6;105(3):593-601. doi: 10.1016/j.bpj.2013.06.041.

Chun J, Zangle TA, Kolarova T, Finn RS, Teitell MA, Reed J. Rapidly quantifying drug sensitivity of dispersed and clumped breast cancer cells by mass profiling. Analyst. 2012 Dec 7;137(23):5495-8. doi: 10.1039/c2an36058f.

Reed J, **Chun J**, Zangle TA, Kalim S, Hong JS, Pefley SE, Zheng X, Gimzewski JK, Teitell MA. Rapid, massively parallel single-cell drug response measurements via live cell interferometry. Biophys J. 2011 Sep 7;101(5):1025-31. doi: 10.1016/j.bpj.2011.07.022.

Chun J, Zangle TA, Reed J, Aiba K, TeSlaa T, Sun C, Gibbs K, Nolan GP, Ho CM, Teitell MA. Quantifying tumor cell responses to therapy with live cell interferometry. NDC Fifth Annual Awardee Meeting Abstracts. 2011 March. Bethesda, Maryland.

Sun C**, Chun J**, TeSlaa T, Aiba K, Gibbs K, Elfmann FL, Krutzik P, Nolan GP, Ho CM, Teitell MA. Attacking signaling complexes to battle leukemia. NDC Fifth Annual Awardee Meeting Abstracts. 2011 March. Bethesda, Maryland.

TeSlaa T, Sun C, **Chun J**, Aiba K, Gibbs K, Elfmann FL, Krutzik P, Nolan GP, Ho CM, Teitell MA. Feedback System Control optimizes drug combination in a preclinical mouse model of acute myeloid leukemia. NDC Fifth Annual Awardee Meeting Abstracts. 2011 March. Bethesda, Maryland.

Wang KC, Li YSJ, Nguyen P, **Chun J** and Chien S. Global analysis of miRNA expression in endothelial cells under different flow patterns [abstract]. 2009 Experimental Biology meeting abstracts, Abstract #776.2; 2009 April. New Orleans, Louisiana.

CHAPTER 1

Introduction

While cell states and responses have often been described by levels of gene expression or protein production, the study of cellular biophysical properties enable another layer of elucidation. Physical properties, such as mass, stiffness, and elasticity, have emerged as an additional perspective to traditional molecular techniques in cellular characterization. These properties can be linked to internal molecular cell processes and further our understanding of cellular response to various diseases and stimuli (1,2). The accessibility of these characteristics to measurement also makes them attractive for assessing larger numbers of single cells and gauging the response of heterogeneous populations.

One of the properties garnering increasing interest, cell mass, can be used to quantify cell size, growth, and motion. Although we know of the involvement of many proteins in the cell cycle, fundamental questions regarding how cells grow throughout the cell cycle and during changes in cell state are still debated in biology. Some believe growth rate to be linked to cell size (larger cells growing at a higher rate than smaller cells), while others find growth rates to be independent of size (3). These different growth curves implicate different regulatory systems to maintain proper cell size throughout the generations, an important consideration to maintain organ structure during cell turnover. Transitions in growth are also seen in instances of changing cell state such as differentiation where cells must alter their growth behavior to take on the role of a more specific cell type (4). Increased study of these mass dynamics can provide a better understanding of the cell cycle and the cause(s) of deviations from expected cell cycle and cell motion behaviors.

Also of interest are changes in cell mass as a measure of cellular fitness. While monitoring cell mass can help find the optimal growing conditions, the reverse may be more interesting. In the case of diseased cells or undesirable cell states in a population, the environment could be perturbed with a stimulus such as a drug and the cells monitored for the desired response (decreased mass or viability of the undesirable subpopulation). In current practice, there is often a standard therapy for a given type of cancer (e.g., cytarabine plus daunorubicin in AML or trastuzumab in HER2+ breast cancer) (5,6,7). This blanket, one-size-fits-all treatment is not always the most effective approach for an individual's cancer.

Current strategies to direct cancer treatment include cell surface marker assays for targeted therapies or, in clinical trials, bulk proliferation assays such as the ATP-luminescence assay for standard chemotherapies (8,9). In these assays, formalin-fixed tissue is immunostained for predictive markers of drug response or dissociated tumor specimens are incubated with prospective drug or drug combination candidates to determine which drugs inhibit proliferation best. Although there is correlation between these in vitro assays and the in vivo patient response, the cell surface markers are not always reliable indicators of sensitivity (7,10) and the assays for traditional chemotherapies are not utilized outside of clinical trials.

Other measures of proliferation, such as cell respiration or colony formation, have also been explored for chemosensitivity assays with updated methods such as electrochemical microscopy and 3D collagen cultures (11,12). While these methods reduce the number of cells required for an assay and improve culture conditions, these proliferation assays are still bulk measurements. They require several days of culture and cannot detect a heterogeneous response to a

treatment. During this lengthy culture period, primary tumor samples are less viable than established cell lines and the assay results only reflect the drug sensitivity of the surviving fraction of tumor cells. Ideally, a chemosensitivity assay should reflect the sensitivity of the entire sample to obtain the best indication of in vivo response possible.

With a live cell mass quantification method, the efficacy of a number of different treatments can be quickly and directly interrogated on a patient sample rather than inferred by the presence or absence of static, partial indicators, such as cell surface markers in pathological specimens. Sensitive mass quantification avoids prolonged culture, allowing the assessment of a drug as it takes effect, while cell viability is at its peak. In this way, an alternate, more effective treatment may be found before applying therapy to the patient, avoiding undue side effects and unwanted disease progression that may make the disease more difficult to treat later on.

Previously, cell size has been estimated through the projected cell area of uniformly shaped cells, such as yeast and bacteria. However, many cell types are irregular in shape, motile, and effected by the environmental osmotic pressure, making projected area a poor measure of size in these instances. Therefore, a more quantitative approach to measuring cell size is necessary and it is only recently that technologies have emerged for quantitative mass measurements for large cell sample populations.

One approach to mass quantification measures the changes in resonant frequency of microelectromechanical systems (MEMS) devices to deduce cell mass. One device consists of a microfluidic channel-embedded cantilever enclosed in a vacuum (13). The microchannel allows for the flow of particles or cells through the length of the cantilever, where the mass of

the particles alters the resonant frequency of the cantilever. This change in frequency can be measured and the buoyant mass of the particle calculated with femtogram precision. This precision makes the resonating cantilevers well suited to the measurement of very small bodies, such as bacteria and single cells, however, the device size must be tailored to the sample. Although these devices have been used to measure the decrease in mass of mouse lymphoblasts due to sodium azide treatment (14), the assessment of a population requires a one-by-one series of measurements or parallelization with cantilevers for each particle, options that are cumbersome and time consuming. Adherent cells and colonies are also not suited to this technique. Partially addressing this gap is a micro fabricated device consisting of an array of square pedestals supported by four springs (15). In this device, cells cultured on the pedestals alter its resonant frequency to determine mass. This allows for adherent cell measurements, but limits cell or colony size to the pedestal dimensions and reduces precision to several picograms due to the submersion of the resonating pedestals in culture medium. Targeting individual cells to the pedestals for parallelization and preventing migration off the pedestal would also pose challenges.

An alternative, optical mass quantification, was explored beginning in the 1950s (16-18) and interference microscopy principles deciphered back then are applicable to optical mass measurement methods in development today. Quantitative phase microscopy techniques generally measure the dry mass of cells by detecting variations in refractive index. Light passed through a sample is compared, by interference, with a reference to determine phase shifts due to the refractive index of the materials encountered by the light, such as cells. The mass can be calculated from this distribution of phase shifts. Multiple methods are in development (19-23) using these principles, differing in details such as imaging speed, method of generating

interference, light transmission or reflection through the sample, and the use of commercially-available or custom modifications to achieve phase images. Digital holography is a variation where both phase and amplitude of scattered light from the sample is recorded in a hologram that can later be digitally processed to remove aberrations and extract phase information to determine the sample mass (22). Another variation, tomographic phase microscopy, is able to record 3D phase information in a z-stack of images that can be used to examine sub-cellular structures instead of just the average phase shift over the entire thickness of the sample (23). Although optical methods like these may require more computational processing, they offer a more flexible approach that is necessary for measurements of both adherent and non-adherent cells, as well as single cells and larger multi-cell colonies. These qualities are advantageous since many cell types, such as certain types of stem cells and various forms of cancer, preferentially grow in aggregates or small multi-cellular clumps.

This dissertation explores live cell interferometry (LCI) as an effective platform for the study and real-time quantification of absolute and changing dry cell mass. The LCI approach is a non-invasive optical mass quantitative method that allows for cellular diversity in shape, size, and growth parameters. First, we establish that LCI is an accurate, longitudinal, wide-field imaging technique that provides a non-invasive and label-free method for quantifying cell mass at single cell and population scale levels of resolution. Then, we have begun to establish potential basic research and translational clinical applications using example systems of drug treatments for HER2+ breast cancer cell lines and quantification of mass accumulation and redistribution in early differentiating human pluripotent stem cells over time.

References

1. Suresh, S. (2007). Biomechanics and biophysics of cancer cells. Acta Materialia, 55(12), 3989-4014.

2. Lee, G. Y., & Lim, C. T. (2007). Biomechanics approaches to studying human diseases. Trends in biotechnology, 25(3), 111-118.

3. Jorgensen, P., & Tyers, M. (2004). How cells coordinate growth and division. Current Biology, 14(23), R1014-R1027.

4. Smith, Z. D., I. Nachman, A. Regev, and A. Meissner. 2010. Dynamic single-cell imaging of direct reprogramming reveals an early specifying event. Nat Biotechnol 28:521-526.

5. Rai, K. R., Holland, J. F., Glidewell, O. J., Weinberg, V., Brunner, K., Obrecht, J. P., ... & Kaan, S. K. (1981). Treatment of acute myelocytic leukemia: a study by cancer and leukemia group B. Blood, 58(6), 1203.

6. Robak, T., & Wierzbowska, A. (2009). Current and emerging therapies for acute myeloid leukemia. Clinical therapeutics, 31, 2349-2370.

7. Vogel, C. L., Cobleigh, M. A., Tripathy, D., Gutheil, J. C., Harris, L. N., Fehrenbacher, L., ... & Press, M. (2002). Efficacy and safety of trastuzumab as a single agent in first-line treatment of HER2-overexpressing metastatic breast cancer. Journal of Clinical Oncology, 20(3), 719-726.

8. Cree, I. A., Kurbacher, C. M., Lamont, A., Hindley, A. C., Love, S., & TCA Ovarian Cancer Trial Group. (2007). A prospective randomized controlled trial of tumour chemosensitivity assay directed chemotherapy versus physician's choice in patients with recurrent platinum-resistant ovarian cancer. *Anti-cancer drugs*, *18*(9), 1093-1101.

9. Konecny, G., Crohns, C., Pegram, M., Felber, M., Lude, S., Kurbacher, C., ... & Untch, M. (2000). Correlation of drug response with the ATP tumorchemosensitivity assay in primary FIGO stage III ovarian cancer. *Gynecologic oncology*, *77*(2), 258-263.

10. Gown, A. M. (2008). Current issues in ER and HER2 testing by IHC in breast cancer. *Modern pathology*, *21*, S8-S15.

11. Yasuda, H., Takada, T., Wada, K., Amano, H., Isaka, T., Yoshida, M., ... & Toyota, N. (1998). A new in-vitro drug sensitivity test (collagen-gel droplet embedded-culture drug sensitivity test) in carcinomas of pancreas and biliary tract: possible clinical utility. *Journal of hepato-biliary-pancreatic surgery*, *5*(3), 261-268.

12. Torisawa, Y. S., Kaya, T., Takii, Y., Oyamatsu, D., Nishizawa, M., & Matsue, T. (2003). Scanning electrochemical microscopy-based drug sensitivity test for a cell culture integrated in silicon microstructures. *Analytical chemistry*, *75*(9), 2154-2158.

13. Godin, M., F. F. Delgado, S. Son, W. H. Grover, A. K. Bryan, A. Tzur, P. Jorgensen, K. Payer, A. D. Grossman, M. W. Kirschner, and S. R. Manalis. 2010. Using buoyant mass to measure the growth of single cells. Nat Methods 7:387-390.

14. Weng, Y., Delgado, F. F., Son, S., Burg, T. P., Wasserman, S. C., & Manalis, S. R. (2011). Mass sensors with mechanical traps for weighing single cells in different fluids. *Lab on a Chip*, *11*(24), 4174-4180.

15. Park, K., L. J. Millet, N. Kim, H. Li, X. Jin, G. Popescu, N. R. Aluru, K. J. Hsia, and R. Bashir. 2010. Measurement of adherent cell mass and growth. Proc Natl Acad Sci U S A 107:20691-20696.

16. Barer, R., Interference Microscopy and Mass Determination. Nature 1952, 169 (4296), 366-367.

17. Davies, H. G.; Wilkins, M. H. F., Interference Microscopy and Mass Determination. Nature 1952, 169 (4300), 541-541.

18. Mitchison, J. M. 1957. The growth of single cells: I. Schizosaccharomyces pombe. Exp. Cell Res. 13:244-262.

19. Reed, J., Chun, J., Zangle, T. A., Kalim, S., Hong, J. S., Pefley, S. E., ... & Teitell, M. A. (2011). Rapid, massively parallel single-cell drug response measurements via live cell interferometry. *Biophysical journal*, *101*(5), 1025-1031.

20. Marquet, P., Rappaz, B., Magistretti, P. J., Cuche, E., Emery, Y., Colomb, T., & Depeursinge, C. (2005). Digital holographic microscopy: a noninvasive contrast imaging technique allowing quantitative visualization of living cells with subwavelength axial accuracy. Optics letters, 30(5), 468-470.

21. Bon, P., Savatier, J., Merlin, M., Wattellier, B., & Monneret, S. (2012). Optical detection and measurement of living cell morphometric features with single-shot quantitative phase microscopy. Journal of biomedical optics, 17(7), 0760041-0760047.

22. Mir, M., Wang, Z., Shen, Z., Bednarz, M., Bashir, R., Golding, I., ... & Popescu, G. (2011). Optical measurement of cycle-dependent cell growth. Proceedings of the National Academy of Sciences, 108(32), 13124-13129.

23. Choi, W., Fang-Yen, C., Badizadegan, K., Oh, S., Lue, N., Dasari, R. R., & Feld, M. S. (2007). Tomographic phase microscopy. Nature methods, 4, 717-719.

CHAPTER 2

Rapid, massively parallel single-cell drug response measurements via live cell interferometry

Interference microscopy is an interesting biophysical approach to measure the spatial distribution of material inside cells and other transparent objects. We have previously shown that an adaptation of this technique, which we call live-cell interferometry (LCI), can sensitively detect and track the nanomechanical properties of hundreds of cells simultaneously (1). LCI can also be used to monitor the dynamic flow of the cytoplasm inside single cells as small indentions are made by highly magnetic probes on the surface of a cell (2). It was found that an almost instantaneous redistribution of cell material resulted from indentation of the cell surface, which was beyond the detection limit of conventional optical microscopy. These results suggest that changes in cell mass could serve as a sensitive, real-time, and non-invasive whole cell marker of cellular fitness. If conducted in a highly parallel fashion, mass measurements could become an effective mechanism for profiling the differential response of cells in a population to internal or external stimuli.

How individual cells regulate their size is poorly understood, as is the relationship between cell mass and well characterized biochemical pathways. Although quantitative mass measurements of single live cells began in the 1950s (3,4), only recently have newer approaches to increase the speed, precision, and practicality of cellular mass measurements become available. For example, a microelectromechanical systems-based approach has been developed to sensitively measure mass changes in a variety of non-adherent cell types flowing sequentially though a hollow microcantilever resonator (5,6). Our own studies with LCI, and the work of others using

optical coherence-based microscopy (7,8), suggests a different, and powerful approach for rapidly, simultaneously, measuring the masses of large populations of cells.

The physical principal underlying LCI is as follows: The variation in phase imparted to coherent or semi-coherent light propagating through a transparent cell body is linearly proportional to the material density of the cell (9–11). Interference microscopy can measure these changes in phase, for micron-sized objects, to precision exceeding 1/1000 of a wavelength, or better than 0.5 nm for visible light. Cell mass can then be related to the measured phase retardation of each cell as (9):

$$m = \frac{1}{\alpha} \int \phi \lambda \, \mathrm{d}A$$

Where m is the mass of the cell, α is a constant describing the relationship between phase shift and cell mass, ϕ is the measured fractional phase shift, λ is the illumination wavelength, and integration is performed across the entire cell area, A. Here, α = 1.8x10^{-3} m^{3}kg^{-1}, consistent with Ross (9) as an average value taking into account the usual contents of a cell. The exact value of α is not known, however, based on previous independent measurements, it is assumed that: 1), α remains constant across a wide range of concentrations and 2), α is not likely to vary $>$ ~5% due to changes in cellular content (9,11,12). Nevertheless, the specific value of α will not affect the accuracy of measurements of comparative growth rates (c.f. **Figs. 2-2** and **2-3**) and relative daughter cell masses after cell division (c.f. **Fig. 2-5**). Fig. 2-1 shows a schematic of the LCI, and typical optical thickness images of adherent and nonadherent cells.

Because it is a wide-field imaging technique, LCI provides simultaneous mass measurements of hundreds of cells (**Fig. 2-2**). Throughout data collection, cells can be maintained in standard culture dishes in physiological conditions (e.g., pH 7.4, 37°C, 5% CO_2) enabling periodic, longitudinal measurements for 6 hours or longer (**Fig. 2-2a**). With an automated image processing algorithm, hundreds of cells can be identified and mass-profiled in each image in rapid succession (**Fig. 2-2b**). In these conditions, the single-cell mass measurements are highly repeatable (<3% CV (coefficient of variation); see Methods: Measurement Errors). At each time point, therefore, the population-wide distribution of cell mass can be determined (**Fig. 2-2c**). Furthermore, individual cells can be tracked over long periods of time to yield growth rate curves (non-aqueous cell mass changes), as in **Fig. 2-2d**.

Results and Discussion

Mass accumulation dynamics have not been previously reported on a cell-by-cell basis over long time scales (several hours) for an entire population of ~100 cells measured simultaneously. To test the hypothesis that LCI mass profiling with can rapidly detect an external cell stimulus, such as a drug response, we exposed H929 multiple myeloma cells to the drug tunicamycin (TM), a protein glycosylation inhibitor (34), and compared the growth profile of TM-treated to untreated control cells by measuring mass continuously over five hours. We determined that the initial distribution of H929 cell masses is approximately log-normal, with a range of 200–700 pg. The majority of cells had mass >200 pg and <400 pg, although a small fraction (3–6%) are much larger than average, with masses above 500 pg.

Both the treated and untreated populations exhibited growth, but the mass accumulation rate was much lower in the treated cells (**Fig. 2-3**). The growth profiles of both populations are

clearly heterogeneous (**Fig. 2-3**, **a** and **b**), and in both, a minority of cells exhibited either a vigorous increase in mass (+15% growth), or little to no mass accumulation (<5% growth). The suppression of growth of the treated population appears within 2 h, and is readily apparent by the fourth hour (**Fig. 2-3**, **c** and **d**). Thus, whole population detection and quantification of cell drug responses were attained within several hours of treatment. The variation in growth rates within the treated and untreated groups (**Fig. 2-3**, **c** and **d**) at 5 h approached the magnitude of the variation between treated and untreated cultures at the same time point. These experiments were conducted on separate days, with distinct subcultures taken from a master stock. Therefore, they are biological not technical replicates, and the difference in behavior likely reflects biological variation. We used technical replicates on controlled samples to estimate the measurement error to be <3% CV (see Methods). Nonetheless, we note that the differences in normalized final mass (final/initial) between each treated sample and each untreated sample are statistically significant with $p < 0.05$ (**Fig. 2-3**, **c** and **d**). This supports the conclusion that the LCI is capable of detecting differences in growth rates between treated and untreated populations of cells.

At the single cell level, the growth rate of individual cells is largely independent of cell mass, within experimental error, for both treated and untreated cells (see **Fig. 2-S1**). An exception is treated population Tm1, which showed a statistically significant linear trend toward slower growth in its larger cell subpopulation. The reason for this difference is unclear. Interestingly, the spread in growth rates within any particular mass fraction cannot be explained entirely by measurement error, suggesting a biological origin of this variation as well. This variation, taken as the norm of the residuals of a linear least squares fit to the growth versus mass data,

ranges from 3.1–5.8% (**Fig. 2-S6**), whereas we estimate the mass measurement error is <3% CV (see discussion of errors in Methods).

To link the kinetics of mass accumulation with biochemical signaling, we profiled molecular markers with PCR and conducted a cell cycle analysis on the treated population. The divergence in growth rates between the treated and untreated populations occurs synchronously with the up-regulation of transcription factors CHOP and the spliced form of XBP1 ('XBP1**-**s'), in the treated population (**Fig. 2-4, a** and **b**). CHOP and XBP1-s activate a host of genes responsible for mitigating the effects of protein mis-folding in the endoplasmic reticulum, through increased production of molecular chaperones to aid protein folding, and accelerated degradation of mis-folded proteins (the so-called unfolded protein response, UPR), and the endoplasmic reticulum-associated protein degradation pathway (35). This is consistent with the known mechanism of TM action (34). Both the UPR and endoplasmic reticulum-associated protein degradation molecular pathways are emerging targets for therapeutic intervention in a wide range of diseases, including multiple myeloma.

XBP1 is a context-dependent positive or negative regulator of cell growth and differentiation in multiple myeloma cells(34). The molecular dynamics of its bipolar transcriptional potential is not well understood. In the context of our experiments, induction of XBP1 mRNA splicing is associated with slowing mass accumulation, but not cell shrinkage or apoptosis. This time-resolved, non-destructive measurement of cell mass greatly helps interpretations of conflicting pro- and anti-proliferate molecular signals, assayed through traditional technique, including immunohistochemistry or quantitative PCR. Cell cycle data show a rapid reduction in the G2/M phase population and a corresponding increase in the G1/G0 population, consistent with cell cycle arrest (**Fig. 2-4c**). This shift becomes pronounced after three hours of TM exposure,

leaving 50% of the cells in G1/G0 by the end of 5 hours of treatment. This is also consistent with observations that activation of the UPR pathway leads to cell cycle arrest (35,36).

We determined the mass range of dividing cells by observing individual divisions and measuring the mass of the parent and daughter cells directly. Twenty-eight cell divisions were observed across all experiments, out of a total of ~600 cells. The number of divisions was skewed in favor of the untreated population 18:11. This is consistent with the observed higher growth rates in that population. The mass at which a cell divides was tightly regulated, and similar in both treated and untreated populations (Fig. **2-5a**). The median mass at division was 515 pg (+/- 75 pg), with the two resulting daughter cells each having a median mass of 250 pg (+/- 40pg). This result enables us to infer via mass values which individual cells in the population are likely to be in early-, mid- and late-phases of the cell cycle. While the mass fraction for the daughter cells was ~50/50 in most instances, a minority of cell divisions were highly asymmetric, with the smaller of the two daughter cells retaining less than 45% of the parent's cell mass (**Fig. 2-5b**). Mass maps of two cells undergoing asymmetric cell division are shown in **Fig. 2-5c**.

There are clear advantages of LCI over other established and emerging methods for single-cell mass measurements. . Unlike hollow cantilever microelectromechanical mass measurement devices (5,6), which require nonadherent cells, LCI is equally compatible with adherent or nonadherent cells (**Fig. 6**). The ability to work with adherent cells is absolutely critical for probing the relationship between mass accumulation/distribution and cell-substrate interactions, and for assessing epithelial or stromal cell types, which form the bulk of human malignancies. LCI is also an excellent approach for linking mass profiling with a whole class of cell

migration, motility, and tissue invasiveness assays commonly used in drug discovery. The interferometric microscope permits full optical access to the specimen, meaning high resolution light micrographs and fluorescent images are easily obtained. This enables the combined use of mass profiling and the extensive armamentarium of fluorescent reporter assays used in cell biology, for simultaneous assessments. Furthermore, LCI demonstrates tracking and quantification of individual cell masses throughout, and following, cell division. To our knowledge, this will directly enable, for the first time, broad spectrum profiling of mass partitioning in stem cells, for example.

LCI is high-throughput and allows longitudinal measurements of the same cells over time; it is also massively parallel, enabling hundreds of longitudinal measurements simultaneously and reducing inter-experiment error due to varying conditions. However, occasionally the conversion from phase to optical thickness is incorrect by a factor of negative one wavelength (530 nm), due to the ambiguity in phase shifts $>2\pi$. This situation causes contiguous regions with the cell to have an apparent optical thickness one wavelength less than the true value. This error is easily detected as a nonphysical discontinuity in optical thickness, and corrected by adding back one wavelength of optical thickness to the affected pixels. This correction process is not currently fully automated, although a substantial body of work addressing this issue exists in the literature (16).

We have measured cell responses to external stimuli for as long as 7 h, and observed unperturbed cultures up to 12 h. In principle, measurements can continue for much longer durations because the cells remain viable for days under tightly controlled culture conditions. One limitation, common to LCI and alternative approaches (5,7,8), is the time required for the

system to stabilize after cells are introduced into the observation chamber, or after media with a different temperature or density is introduced. In the present experiments, we have conservatively allowed 1 h of settling time, although if required this settling time could be reduced by at least a factor of two.

In summary, high throughput LCI mass profiling is a sensitive and precise mechanism for quantifying single cell, population-based responses to environmental perturbations, such as medically relevant drug responses.

Materials and Methods

Interferometer. The live cell interferometer has been described in detail previously (1). Briefly, the system is an optical microscope, based on a modified Veeco NT9300 optical profiler, with a 20X 0.28NA Michelson interference objective that allows for the observation of not only lateral features with typical optical resolution (1.16 μm for the 20x objective) but also height dimensions of reflective objects below the scale of one nanometer. The Michelson interferometer is composed of a beam splitter, reference mirror and compensating fluid cell to adjust for optical path differences induced by fluid surrounding the specimen. The phase shifting interferometry (PSI) (14) method was used to capture phase images of the cell bodies *in situ*. During measurement, a piezoelectric translator decreases the light path a small amount causing a phase shift between the test and reference beams. The system records the irradiance of the resulting interference pattern at many different phase shifts and then converts the irradiance to phase wavefront data by integrating the irradiance data using a PSI algorithm. As currently implemented, the autofocus and PSI measurement cycle takes 12 s. The PSI measurement itself takes 1–2 s, and is limited by the camera frame rate (60 fps). In our

present experiments, one set of 25 images, containing 400–1000 cells, was captured every 7 min. Each set of 25 images contained hundreds of cells, with data from the first five images presented here, and therefore each run includes ~80 cells. All cells within each of the selected images were measured.

Data analysis. The software native to the Bruker NT9300 (Bruker, Tucson, AZ) allows automated optical thickness measurements of cells selected manually from the phase image. The optical thickness is converted to mass as described in the text, using the conversion constant, α = 1.8x10^{-3} m^{3}kg^{-1}, consistent with Ross (9). The boundary of each cell was automatically selected by an algorithm that partitions objects from the background using a threshold determined from the histogram of pixel heights (15). Conversion of the raw phase image into optical thickness uses a series of well-established phase unwrapping routines (16). Occasionally, this conversion from phase to optical thickness is incorrect by a factor of negative one wavelength (530 nm), which causes contiguous regions with the cell to have an apparent optical thickness one wavelength less than the true value. This error is easily detected as a nonphysical discontinuity in optical thickness, and corrected by adding back one wavelength of optical thickness to the affected pixels. This process is not currently fully automated.

Measurement Errors. The accuracy of interference microscopy for cell mass measurements is firmly established in the electromagnetic theory (17,18), and by a variety of reference techniques that include ultracentrifugation (3,4,10–12,19–21), refractometry of protein solutions, hydrogels, and transparent films (22–24), x-ray densitometry (25), and electron microcopy (26–30). To char- acterize the accuracy and stability of our LCI system, we conducted

several benchmark experiments, the detail for which is given in the Supporting Material, see Fig. S2, Fig. S3, Fig. S4, and Fig. S5. The lower limit of CV for LCI mass measurements, which is a function of the temporal stability of the interferometric optical path (1.2 Å ; **Fig. 2-S2 a**), was determined to be ~0.35%. Similar CVs were determined for serial measurements of partially melted polystyrene beads, which simulated cells (CV $<$ 0.4%;**Fig. 2-S2 b**), and for short repeated measurements of actual live cells (CV $<$1%; **Fig. 2-S3**). We measured populations of 6 mm diameter polystyrene spheres (**Fig. 2-S4 a**) normally used as calibration standards in flow cytometry (Flow Check, Polysciences), and for which a population mean volume and standard deviation are provided by the manufacturer; the population mass CV determined by LCI (6.8%) was considerably smaller than that determined by the manufacturer (15%). We also measured a population of red blood cells (RBCs) freshly obtained from a 15-week-old female C57BL/6 mouse (**Fig. 2-S4**, **b** and **c**). Mouse RBCs serve as an informative independent standard because there exits an established range of values for average cell mass (determined by photochemical and other methods). Our LCI-determined value of mean RBC cell mass, 19.4 pg, are in excellent agreement with the range of published values at 15–21 pg (9–12,31). Finally, for comparison we measured the masses of populations of a variety of mammalian cell types (**Fig. 2-S4 b** and **Fig. 2-S5**). These are plotted together with the mouse RBC and polystyrene sphere data in the Supporting Material and **Fig. 2-3 b**. To estimate the scale of measurement variation in multi-hour live cell experiments, all single-cell mass versus time data, (representing ~480 cells) were fitted to a simple exponential growth model ($mass(t) = m_0 * C^t$, where the constant C is close to unity) and residual error calculated as the percent difference between the trend and the actual data at each time point (**Fig. 2-S6 a**). The residuals are symmetrically distributed about zero (**Fig. 2-S6 b**) and the range between the 25% and 75% quartile varies from 0.0126 (c2) to 0.027 (c3); the mean interquartile range was

0.02. Taken together, these results indicate a lower bound of measurement repeatability on the order of 0.5–1.0% and an outer bound of 2.0–3.0%. The main difference between short- and long-term measurements of live cells is the shape change that occurs over the scale of hours. This can cause added variation in the integrated optical thickness from: 1), small errors in partitioning the cell boundaries; 2), optical averaging of closely spaced fringes present at the edge of rounded cells; and 3), a potential change in the value of α, the mass-to-optical thickness constant, although previous work suggests this error would be relatively small (3). It is established that 1), α is unaffected by changes in concentration, even up to the limit of crystallized protein solutions (9); 2), α reflects the mass interacting with light at a specific location (9–12,31) and is, therefore, not affected by how much area the cell occupies within the field of view as it grows; and 3), the value of α remains close to 0.0018 over a wide range of materials found in cells (32).

Cell lines and tissue culture. H929 human multiple myeloma cells were maintained at 37°C in 5% CO_2 in RPMI 1640 growth medium supplemented with 10% defined fetal bovine serum (HyClone) and antibiotics. The observation chamber was 4.5 cm in diameter and 1.5 cm deep with a 2 $\times$ 2 cm silicon substrate placed on top of a plastic shelf such that the silicon was near the top of the fluid surface. The imaging cell was completed by a piece of optical glass (BK7 glass, Quartz Plus, Brookline, NH) separated from the silicon surface by resting on top of three 600 μm stainless steel beads (Salem Specialty Ball Company, Canton, CT) to create a uniform thickness sample chamber. Media bubbled with 5% CO_2 air was continuously flowed through the incubation chamber using a peristaltic perfusion pump at a rate of 0.5 ml/min. The 530 nm wavelength LED illumination (Luxeon Star LED, Brantford, Ontario) incident on the sample chamber had a power of 15 μW spread over a 1.2 mm diameter illumination spot. We have

measured cell responses to external stimuli for as long as 7 h in this configuration, and observed unperturbed cultures for up to 12 h, although the upper limit of experiment duration has not been determined.

Drug treatment, cell cycle analysis, and nucleic acid isolation. H929 cells were seeded in 6-well culture plates at a density of $1x10^6$ cells/well. Before plating cells in the LCI's observation chamber, either 1 ml of Tunicamycin (TM) (T7765; Sigma-Aldrich) in dimethyl sulfoxide(DMSO), or DMSO alone were added to the media at a concentration of 10 mg/ml, DMSO/media (1:1000 dilution). Mass measurements commenced 1 h after the cells were plated in the observation chamber to allow the experimental system to stabilize, i.e., culture acclimation, temperature stabilization, etc. For cell cycle analysis, cells from each time point were collected and incubated with a hypotonic DNA-staining buffer containing propidium iodide and later analyzed by flow cytometry. RNA for each time point was extracted using the Trizol reagent (Invitrogen).

Reverse transcription, RT-PCR, and quantitative RT-PCR. cDNA was synthesized from 3μg of total RNA with oligo(dT) primers using the Superscript III first strand cDNA synthesis kit (Invitrogen). RT-PCR for *XBP1* spliced and unspliced forms was performed using Platinum Taq (Invitrogen) at an annealing temperature of 58° C for 25 cycles. Quantitative RT-PCR for *CHOP (DDIT3)* mRNA was performed using SYBR green real time PCR kit (Diagenode) and an Applied Biosystems (Foster City, CA, USA) 7700 sequence detector as described (33). Samples were analyzed for *36b4* expression as a normalization control. Primer sequences are available on request.

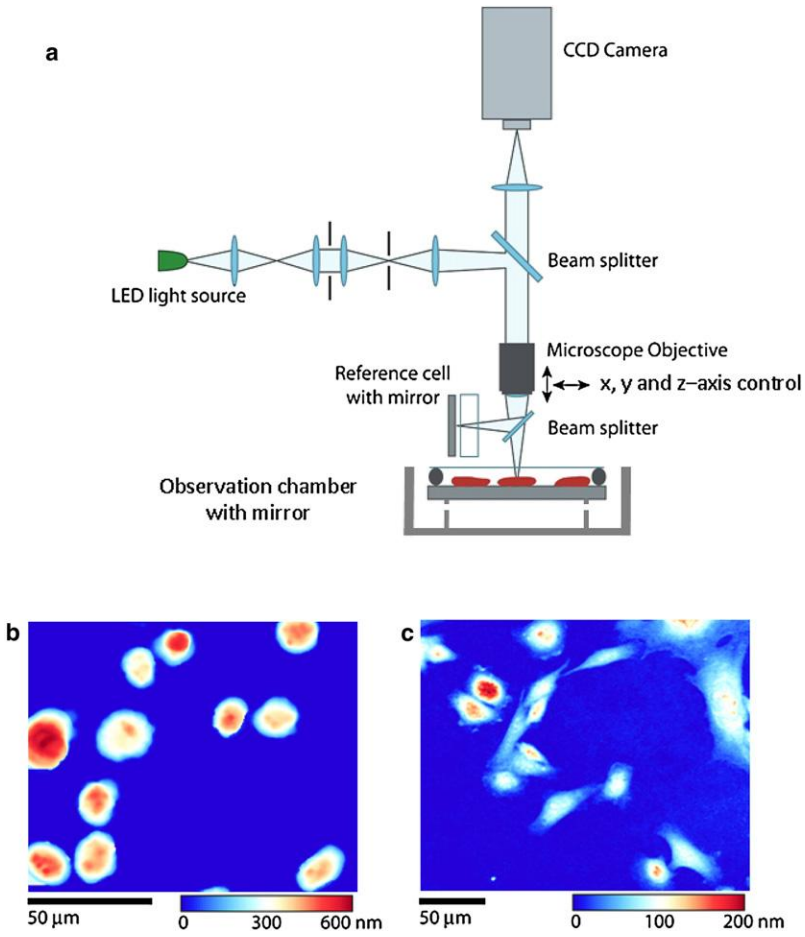

Figure 2-1. Live cell interferometer (LCI). The LCI (**a**) is a Michelson-type interference microscope that compares the optical thickness of a reference cell to the optical thickness of samples placed in the observation chamber. Suspended in the observation chamber is a mirrored substrate, allowing the LCI to make measurements of optical thickness on transparent cells. The relative position of the microscope objective and observation chamber is controlled by computer and translatable in three-dimensions allowing for rapid, automated image acquisition. Throughout data collection, cells in the observation chamber are maintained in standard cell culture conditions (e.g., pH 7.4, 37°C, 5% CO_2). The LCI is capable of measuring the mass of both adherent and non- adherent cells. Frame (**b**) shows several non-adherent H929 cells attached to the observation chamber substrate after coating the substrate

with Poly-L-Lysine solution, whereas frame (**c**) shows adherent female Indian Muntjac (9) cells cultured directly on the substrate. The color maps show optical thickness measurements with blue being a low optical thickness relative to background and red being a high optical thickness.

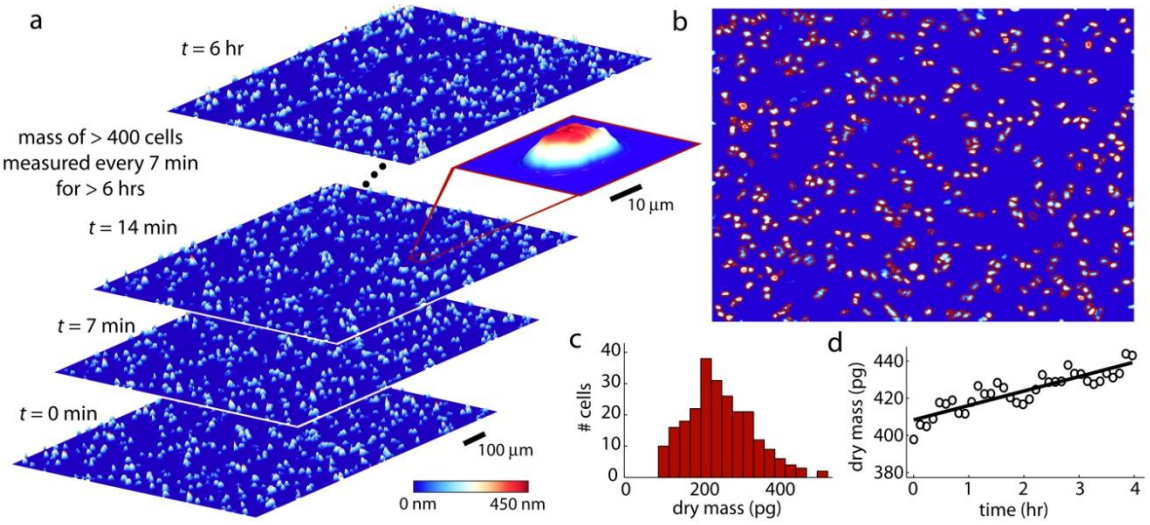

Figure 2-2. LCI enables high-throughput and longitudinal measurements of cell mass. (**a**) Four sample images of H929 multiple myeloma cells from the LCI show optical thickness profiles of cells over 6 hours of monitoring. Color indicates phase shift in nm, with dark blue indicating low thickness and white/red indicating high thickness. These sample images are composites of 25 successive CCD captures taken every 7 minutes. The inset shows a measurement of the phase shift across a single cell. Integrated phase shift across a cell is directly proportional to cell dry mass. (**b**) Hundreds of individual cells (outlined in red) are identified at unique positions in each frame and (**c**) the mass of each individual cell is determined, enabling high-throughput, population-level mass profiling over time. (**d**) The mass of individual cells is tracked longitudinally over time to examine single cell growth dynamics. Measurements are shown as open symbols with a linear least squares best fit line.

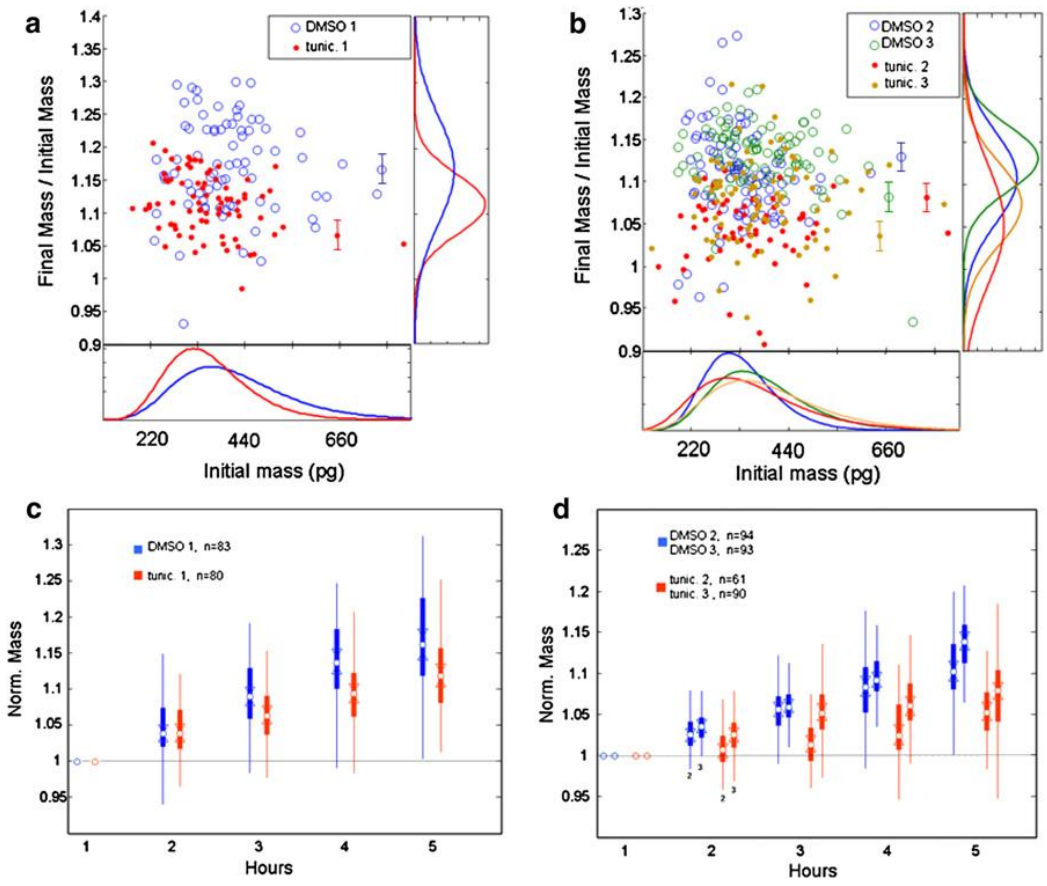

Figure 2-3. Drug response of H929 multiple myeloma cells profiled by single-cell mass accumulation: Results of LCI longitudinal mass measurements on populations of H929 multiple myeloma cells, comparing the mass accumulation of DMSO-treated controls with TM-treated (10 mg/ml) cells. Data are taken over 5 h as described in Methods. The treated cells grow more slowly than do the controls. Experiments Nos. 2 and 3 were conducted at 32°C vs. 37°C for No. 1, which accounts for the slightly lower overall growth rates observed. The scatter plots (**a** and **b**) depict the growth of individual cells at 5 h versus their initial mass (normalized by initial mass). Error bars represent52% CV, our estimate of the measurement error (see Methods). Error bars apply to all data, but are omitted for the majority of points in the plot for clarity. In the box plots of normalized mass versus time (**c** and **d**), circles indicate the sample median, and triangles indicate the 95% confidence interval for the median. Solid boxes indicate

limits of the 25 and 75 percentiles, and whiskers represent two standard deviations from the mean.

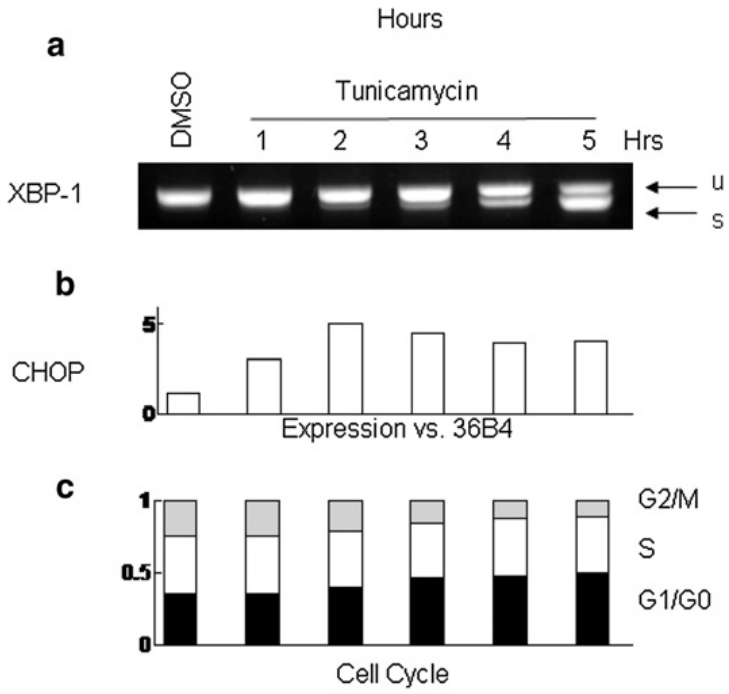

Figure 2-4. Molecular profile of H929 response to TM. The divergence in growth rates between the treated and untreated populations occurs synchronously with the up-regulation of the transcription factor CHOP (**a**) and the alternative splicing of transcription factor XBP1 (**b**) in the treated population. CHOP and XBP1-s activate a host of genes responsible for mitigating the effects of protein misfolding in the endoplasmic reticulum. This is consistent with the known mechanism of TM action, an inhibitor of protein glycosylation. (**c**) Cell cycle data show a rapid reduction in the G2/M phase population and a corresponding increase in the G1/G0 population, consistent with cell cycle arrest. This shift becomes pronounced after 3 h of treatment, leaving 50% of cells in G1/G0 by the end of 5 h of treatment.

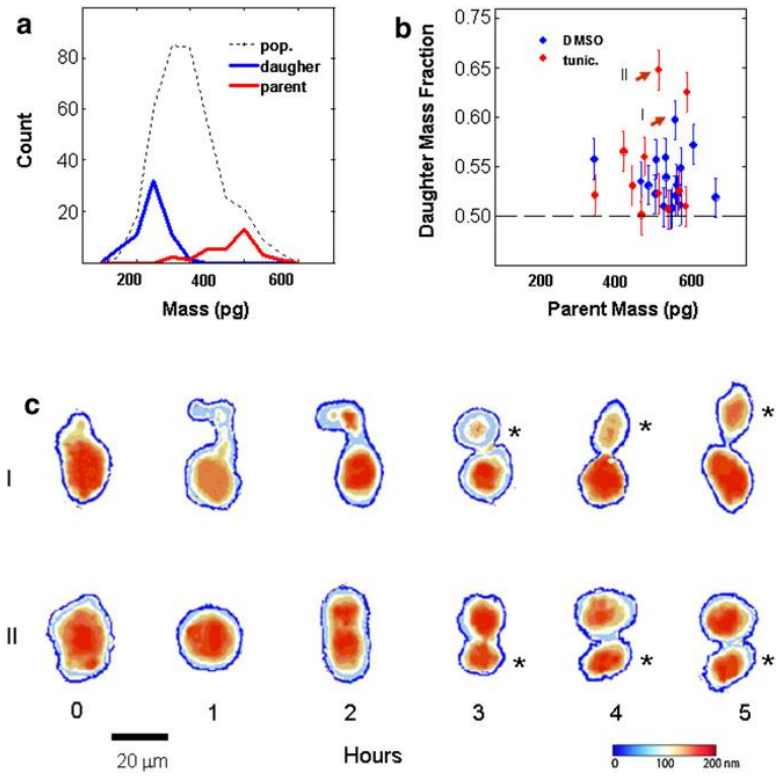

Figure 2-5. Mass dynamics of cell division. Twenty-eight cell division events were recorded from the treated and untreated populations in all experiments (from a total of ~600 cells). (**a**) We determined the mass range of dividing cells by observing individual divisions and measuring the mass of the parent and daughter cells directly. Panel (**a**) compares the mass distribution of all cells measured (both treated and untreated; dashed line) with the masses of those cells which divided during the experiment (red before division, blue after division). (**b**) Surprisingly, a number of cells divisions were highly asymmetric, with ~45%, or less, of the total parent cell mass remaining in the smaller of the two daughter cells. (**c**) Two examples of highly asymmetric division are shown over the five hour time course. The smaller of the daughter cells in these divisions (indicated by an asterisk) contained 35% and 40% respectively, of the parent cell mass. These division events are indicated by red-filled circles in (**b**). Error bars represent 52%CV, our estimate of the measurement error (see Methods).

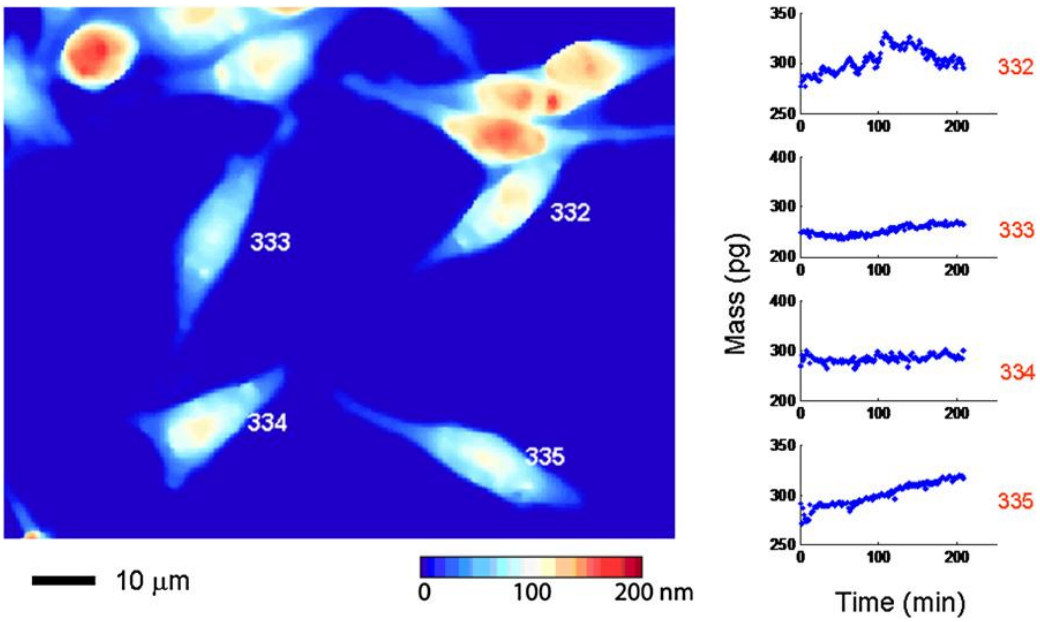

Figure 2-6. Live cell interferometer measures the mass of adherent cells: Frame shows several mouse fibroblast cells cultured directly on a polished silicon substrate. The color map indicates optical thickness measurements with blue being a low optical thickness relative to background and red being a high optical thickness. To the left are mass measurements of the four cells, as indicated, taken every 2 s for 200 min. The smaller optical thickness of the adherent cells versus non-adherent cells is easily measured by the LCI.

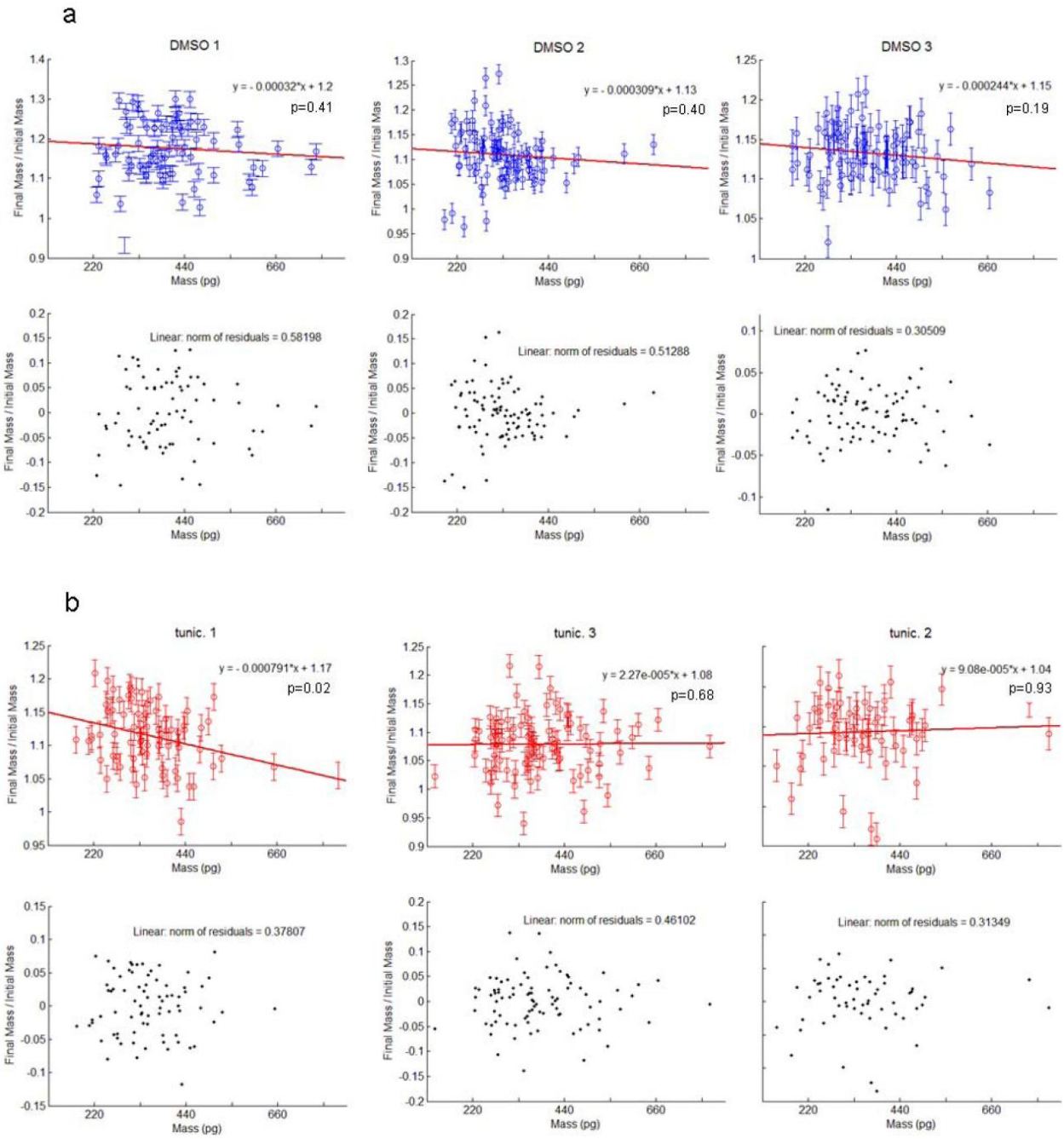

Figure 2-S1. Scatter plots of treated and untreated data sets. The red trend line represents a linear least-squares fit to the data. The p value, indicating the probability that there is no correlation between growth rate and cell mass, is given for each fit. There is a trend toward a slower growth as cell mass increases in the untreated controls, although this is not statistically

significant to 95% confidence. The treated sets Tm2 and Tm3 show no correlation between growth rate and mass, while the negative slope is significant ($p=0.02$) for Tm1. The norm of the residuals for each linear fit provides an estimate of growth variation within each mass segment. Error bars represent +/- 2% CV, our estimate of the measurement error (see Methods).

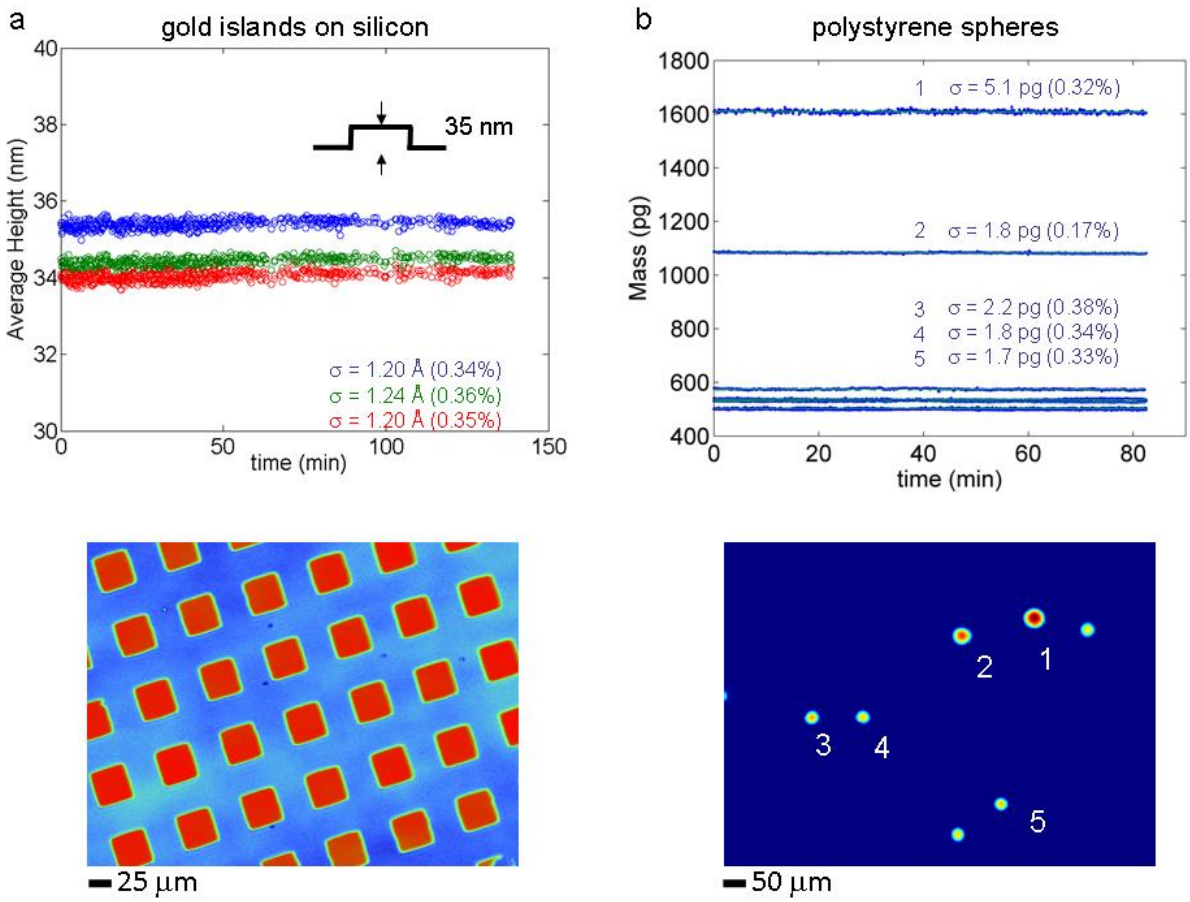

Figure 2-S2. Optical path and mass measurement stability of LCI. Gold islands vapor deposited onto silicon (**a,** lower panel), ~35 nm in height, were measured repeatedly for 140 minutes to test the stability of the interferometer. Shown in the top panel, the mean height of three representative islands shows no meaningful drift during this period and the measurement repeatability, given as the standard deviation of the height, is ~1.2 angstroms or 0.35% of the total height. Similarly, stability of the mass measurement for transparent objects is estimated by repeatedly measuring partially-melted 10 um diameter polystyrene spheres (**b**) over 80+ minutes. In the top panel, trace #1 represents three spheres melted into a cluster, and trace #2 represents two spheres melted into a cluster. The other three traces are from single spheres. The coefficient of variation of the mass measurement for the polystyrene spheres is similar to

that obtained for the mean height of the gold islands, <0.4%, with negligible drift over the measurement period. Data were collected in the LCI observation chamber under conditions identical to those used to measure live cells, with the exception that water replaced the culture medium.

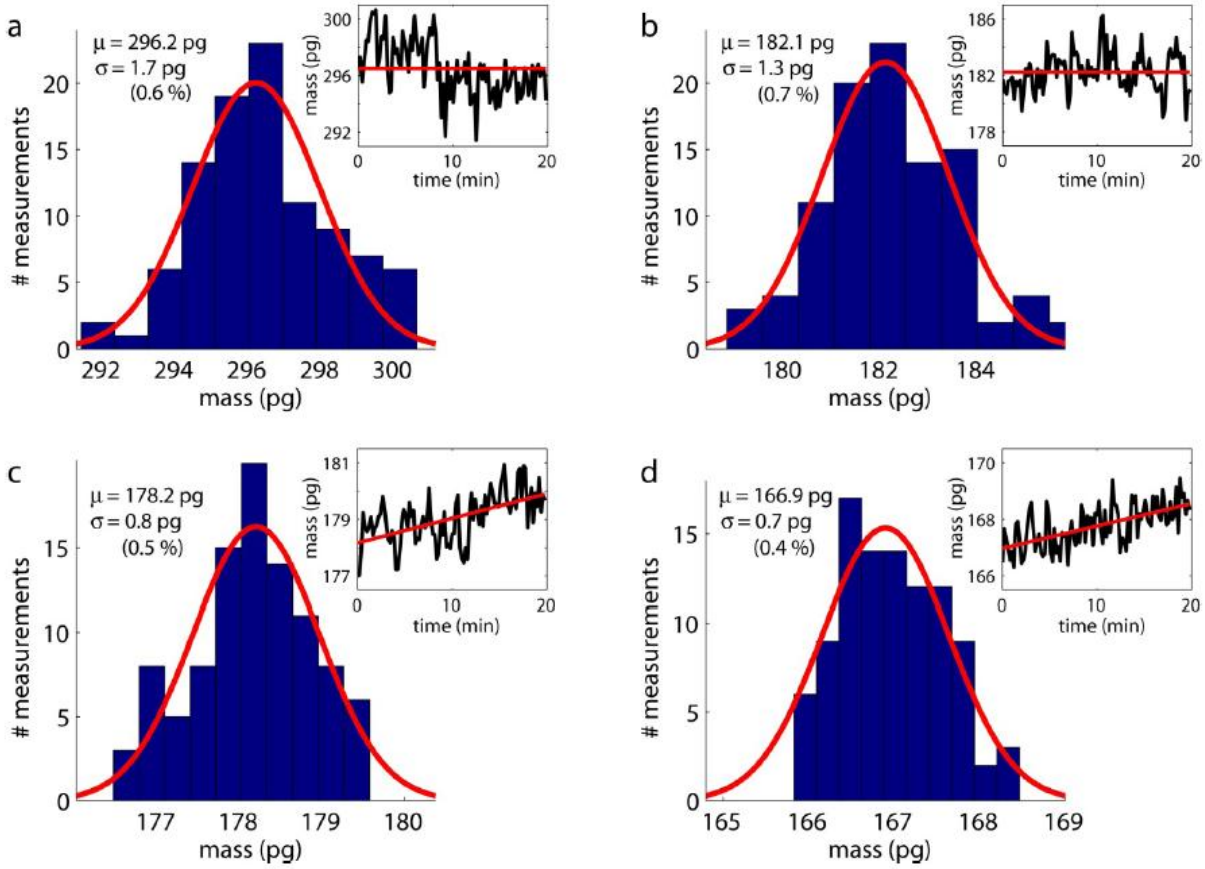

Figure 2-S3. LCI measures mass with high precision. Four individual cells (**a** through **d**) were selected and tracked over 98 successive measurements made at roughly 12 s intervals. Over this time period (20 min total) the observed cells showed small changes in mass (see inset plots of mass vs. time), allowing assessment of measurement repeatability. Cells in **c** and **d** show > one picogram average mass change over this period, so histograms in **c** and **d** present measured mass minus the linear component of the least-squares fit line (shown in red in the inset) to remove any additional variance due to growth. Histograms of measurements for each cell were fitted to a Gaussian distribution by nonlinear least squares fitting in Matlab. Mean (μ) and standard deviation (σ) are reported for each distribution. All standard deviations are <1% of the distribution mean indicating that mass measurements with the LCI are highly repeatable.

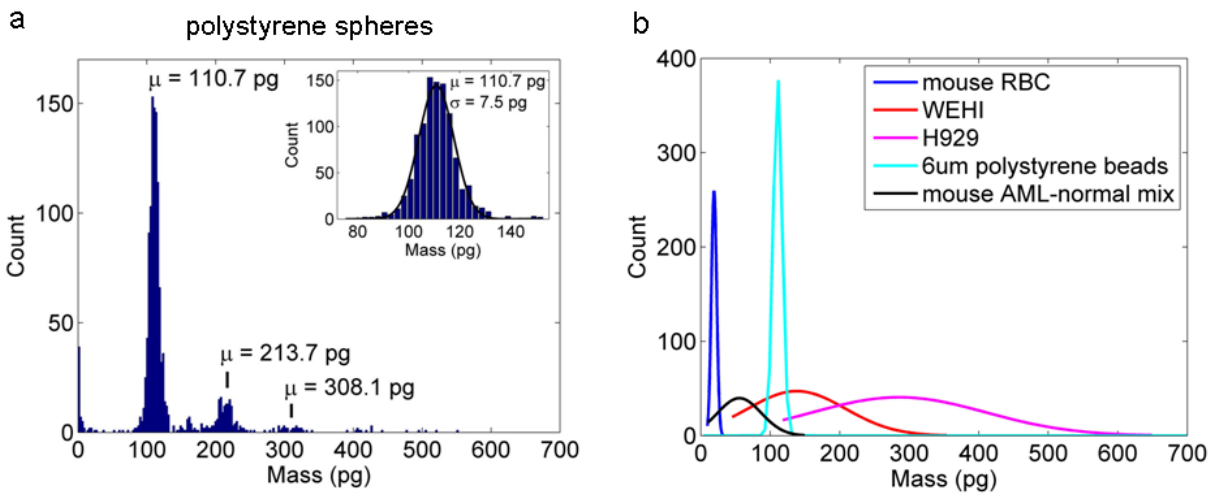

c mouse RBC mass / mean corpuscular hemoglobin (MCH)

authors	ave mass (pg)	MCH (pg)	technique
Nie *et al*	18.4	16.2	mass spec / photochemical
Magnani *et al*	20.3	17.9	photochemical
Wirth-Dzięciołowska et al	15.7-20.7	13.8-18.3	photochemical
Vaysse *et al*	16.9-20.7	15-21	photochemical
Mysliwsk & Lass	18.5	16.3	interferometry
This work	**19.4**	**17.1**	**interferometry**

Figure 2-S4. The mass of a population of partially melted 6 um diameter polystyrene spheres (Flow Check, Polysciences Inc.) were measured by LCI in water (**a**). During preparation the spheres infrequently aggregate and upon heating dimers and trimers coalesce into single, conical clusters. Peaks for the population of monomers (110.7 pg), dimers (213.7 pg) and trimers (308.1 pg) can be distinguished in the histogram. The LCI-measured standard deviation of the monomer population mass is 7.5 pg, or 6.8% of the mean, which exceeds the manufacturers' stated specification of 15%. The mass distribution of populations of four different mammalian cells types and the 6 um polystyrene spheres are plotted together as histograms for comparison (**b**). The mean mass of the mouse red blood cell (RBC) population determined with LCI can be compared to published values determined by other techniques 1-4, and by another group using microinterferometry 5 (**c**). Nie et al measured the cell mass of

mouse RBCs using a novel mass spectrometric method, and also the mean corpuscular hemoglobin mass (MCH) by traditional photochemical techniques1. The MCH typically represents a large fraction of the total cell mass of mammalian red blood cells. The range of MCH values for various mouse strains are well established2, 4, 5. Using the ratio of MCH-to-total mass given by Nie et al as an estimate, we can compare the established values for mouse RBC MCH to the average mouse RBC mass measured in this study. The estimated values are displayed in red.

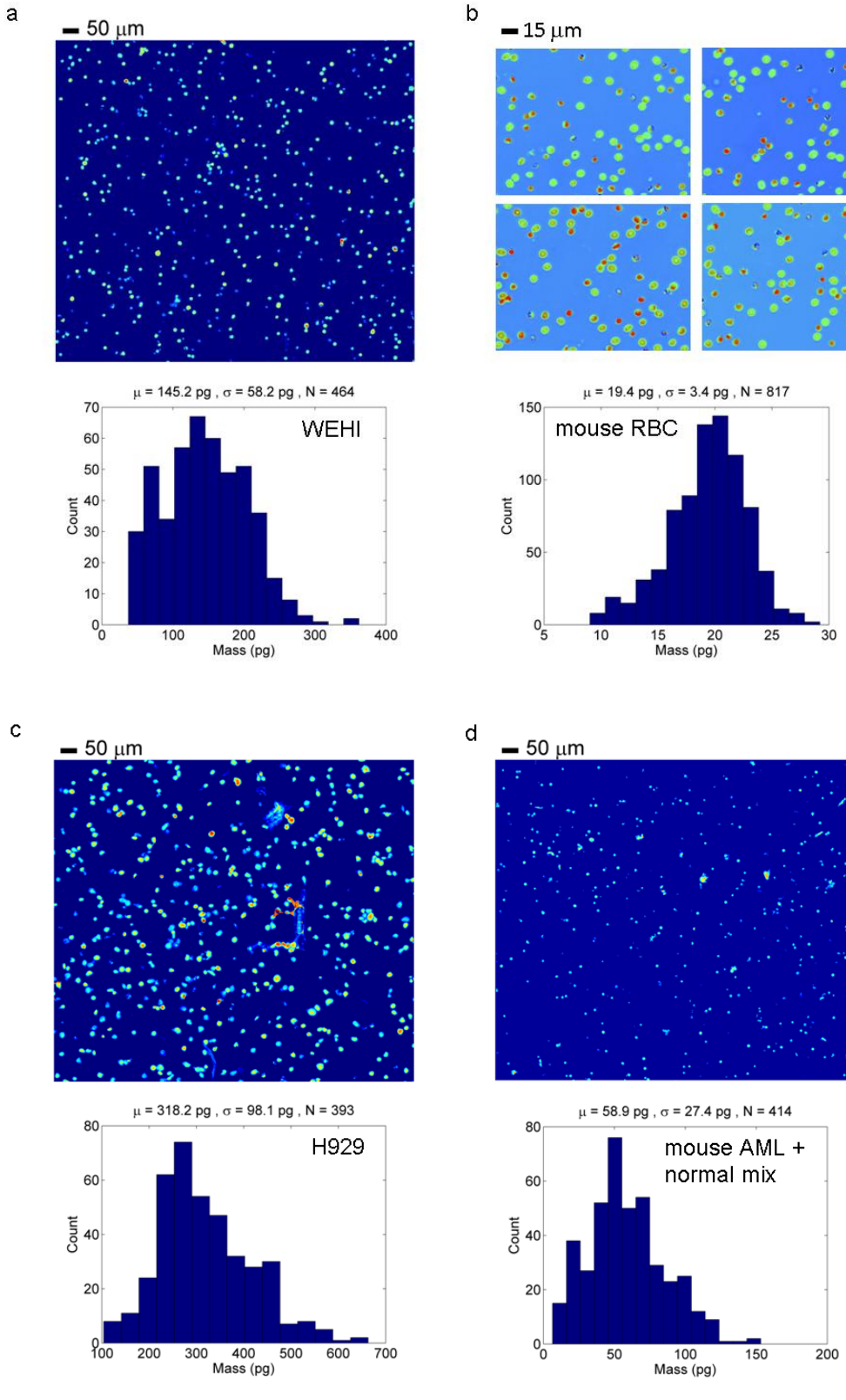
a
50 μm
μ = 145.2 pg , σ = 58.2 pg , N = 464
WEHI
Count
Mass (pg)
b
15 μm
μ = 19.4 pg , σ = 3.4 pg , N = 817
mouse RBC
Count
Mass (pg)
c
50 μm
μ = 318.2 pg , σ = 98.1 pg , N = 393
H929
Count
Mass (pg)
d
50 μm
μ = 58.9 pg , σ = 27.4 pg , N = 414
mouse AML +
normal mix
Count
Mass (pg)

Figure 2-S5. The mass distributions of populations of four different live or freshly prepared cell types were measured by LCI: (**a**) mouse WEHI-231 B lymphoma cells (**b**) red blood cells (RBCs) from a 15 week-old female C57BL/6 mouse, (**c**) human H929 multiple myeloma cells, and (**d**) a mixture of primary bone marrow and acute myeloid leukemia (AML) cells established in a C57BL/6 mouse by retroviral transduction and adoptive cell transfer using standard techniques.

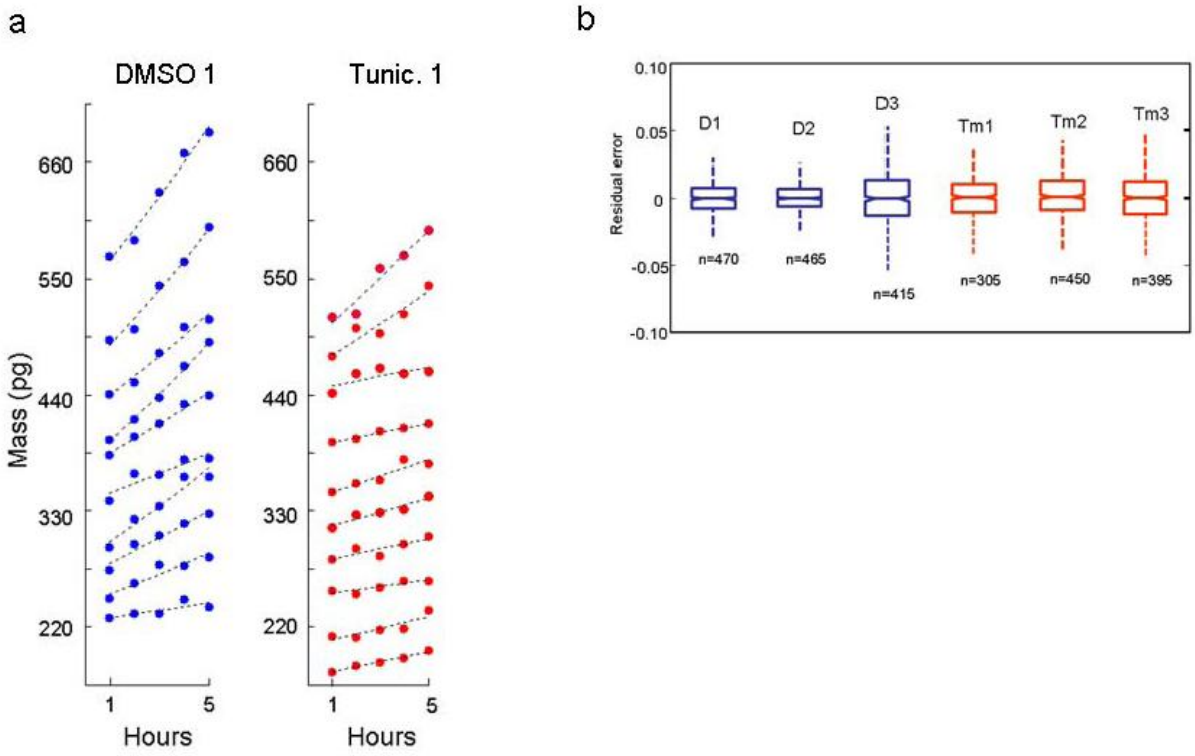

Figure 2-S6. Mass vs. time plots (**a**) for representative cells from the data given in **Fig. 3 a** in the main text. The dashed lines represent an exponential growth fit to the data. To estimate the scale of measurement variation in the live cell experiments, all single-cell mass vs. time data, from all three Tm-treated and DMSO control runs (indicated D1-D3 and Tm1-Tm3, respectively), were fitted to a simple exponential growth model (mass(t)=m0*Ct , where the constant C is close to unity), and residual error calculated as the percent difference between the trend and the actual data at each time point. In the box plot (**b**), the central line indicates the sample median, and triangles indicate the 95% confidence interval for the median. Solid boxes indicate limits of the 25 and 75 percentiles, and whiskers represent two standard deviations from the mean. The residuals are symmetrically distributed about zero, and the range between the 25% and 75% quartile (IQR) varies from 0.0126 (D2) to 0.027 (D3). The mean IQR is 0.02.

References

1. Reed, J., M. Frank, …, J. K. Gimzewski. 2008. High throughput cell nanomechanics with mechanical imaging interferometry. Nanotech- nology. 19:235101.

2. Reed, J., J. J. Troke, …, J. K. Gimzewski. 2008. Live cell interferometry reveals cellular dynamism during force propagation. ACS Nano. 2:841–846.

3. Barer, R., and S. Joseph. 1954. Refractometry of living cells. Part 1. Basic principles. Q. J. Microsc. Sci. 95:399–423.

4. Davies, H. G., M. H. F. Wilkins, …, L. F. Lacour. 1954. The use of the interference microscope to determine dry mass in living cells and as a quantitative cytochemical method. Q. J. Microsc. Sci. 95: 271–304.

5. Godin, M., F. F. Delgado, …, S. R. Manalis. 2010. Using buoyant mass to measure the growth of single cells. Nat. Methods. 7:387–390.

6. Bryan, A. K., A. Goranov, …, S. R. Manalis. 2010. Measurement of mass, density, and volume during the cell cycle of yeast. Proc. Natl. Acad. Sci. USA. 107:999–1004.

7. Park, Y. K., M. Diez-Silva, …, S. Suresh. 2008. Refractive index maps and membrane dynamics of human red blood cells parasitized by Plasmodium falciparum. Proc. Natl. Acad. Sci. USA. 105:13730–13735.

8. Popescu, G., Y. Park, …, K. Badizadegan. 2008. Optical imaging of cell mass and growth dynamics. Am. J. Physiol. Cell Physiol. 295: C538–C544.

9. Ross, K. F. A. 1967. Phase Contrast and Interference Microscopy of Cell Biologists. Edward Arnold, London, UK.

10. Barer, R. 1952. Interference microscopy and mass determination. Nature. 169:366–367.

11. Davies, H. G., and M. H. F. Wilkins. 1952. Interference microscopy and mass determination. Nature. 169:541.

12. Barer, R., K. F. A. Ross, and S. Tkaczyk. 1953. Refractometry of living cells. Nature. 171:720–724.

13. Reference deleted in proof.

14. Schmit, J., and K. Creath. 1996. Window function influence on phase error in phase-shifting algorithms. Appl. Opt. 35:5642–5649.

15. Otsu, N. 1979. A threshold selection method from gray-level histograms. IEEE Trans. Syst. Man Cybern. 9:62–66.

16. Ghiglia, D., and M. Pritt. 1998. Two-Dimensional Phase Unwrapping: Theory, Algorithms, and Software. John Wiley & Sons, Hoboken, NJ.

17. Adair, G. S., A. G. Ogston, and J. P. Johnston. 1946. Osmotic pressures and sedimentation velocity of Gastrophilus methaemoglobin. Biochem. J. 40:867–869.

18. Pedersen, K. O. 1936. Ultracentrifugal and electrophoretic studies on the milk proteins: the lactoglobulin of Palmer. Biochem. J. 30:961–970.

19. Adair, G. S., and M. E. Robinson. 1930. The specific refraction increments of serum-albumin and serum-globulin. Biochem. J. 24:993–1011.

20. Davies, H. G. 1958. On microscope interferometry and the specific refraction increment of a crystalline protein. J. Histochem. Cytochem. 6:393.

21. Barer, R., and S. Joseph. 1955. Refractometry of living cells. 3. Technical and optical methods. Q. J. Microsc. Sci. 96:423–447.

22. Grampp, W., O. Hallen, and B. Rosengren. 1960. Mass determination by interference microscopy and x-ray microscopy. A comparative study. Exp. Cell Res. 19:437–442.

23. Gamble, C. N., and D. Glick. 1960. Determination of the total dry mass of human erythrocytes by interference microscopy and x-ray microradiography. J. Histochem. Cytochem. 8:332–333.

24. Ottoson, R., K. Kahn, and D. Glick. 1958. Studies in histochemistry. 48. Dry mass of mast cells measured by interference microscopy and x-ray absorption. Exp. Cell Res. 14:567–574.

25. Ruch, F., and G. F. Bahr. 1970. Dry mass determination by interference microscopy; agreement with quantitative electron microscopy. Exp. Cell Res. 60:470.

26. Magnani, M., L. Rossi, …, G. Fornaini. 1988. Effect of age on some properties of mice erythrocytes. Mech. Ageing Dev. 42:37–47.

27. My sliwski, A., and P. Lass. 1985. Increase of size and dry mass of mouse erythrocytes depending on age of donors. Mech. Ageing Dev. 29:107–110.

28. Nie, Z., F. Cui, …, A. L. Yu. 2007. High-speed mass analysis of whole erythrocytes by charge-detection quadrupole ion trap mass spectrometry. Anal. Chem. 79:7401–7407.

29. Vaysse, J., R. Vassy, …, P. Pilardeau. 1988. Does red blood cell size correlate with red blood cell age in mouse? Mech. Ageing Dev. 44:265–276.

30. Wirth-Dzieciolowska, E., J. Karaszewska, …, M. Gajewska. 2009. Selected peripheral blood cell parameters in twelve inbred strains of laboratory mice. Anim. Sci. Pap. Rep. 27:69-77.

31. Barer, R. 1957. Refractometry and interferometry of living cells. J. Opt. Soc. Am. 47:545–556.

32. Dawson, D. W., J. S. Hong, …, M. A. Teitell. 2007. Global DNA methylation profiling reveals silencing of a secreted form of Epha7 in mouse and human germinal center B-cell lymphomas. Oncogene. 26:4243–4252.

33. Lee, J. Y., M. Koi, …, A. P. Feinberg. 1994. Simple purification of human chromosomes to homogeneity using muntjac hybrid cells. Nat. Genet. 7:29–33.

34. Shaffer, A. L., M. Shapiro-Shelef, …, L. M. Staudt. 2004. XBP1, downstream of Blimp-1, expands the secretory apparatus and other organelles, and increases protein synthesis in plasma cell differentiation. Immunity. 21:81–93.

35. Brewer, J. W., and J. A. Diehl. 2000. PERK mediates cell-cycle exit during the mammalian unfolded protein response. Proc. Natl. Acad. Sci. USA. 97:12625–12630.

36. Brewer, J. W., L. M. Hendershot, …, J. A. Diehl. 1999. Mammalian unfolded protein response inhibits cyclin D1 translation and cell-cycle progression. Proc. Natl. Acad. Sci. USA. 96:8505–8510

CHAPTER 3

Rapidly quantifying drug sensitivity of dispersed and clumped breast cancer cells by mass profiling

Last year (2011) in the United States, 230,480 women were diagnosed with breast cancer and 39,520 women died from the disease. (1) The clinical course and outcome for this common malignancy remains variable despite therapies that are usually guided by a combination of clinical assessments, including tumor subtype, clinical grade and stage, and the expression of estrogen (ER), progesterone (PR), and amplified HER2 cell surface receptors. (2, 3) Unfortunately, breast cancers expressing ER, PR, and/or amplified HER2 surface receptors do not always respond to therapies that target these receptor-linked pathways, making the analysis of expression of these biomarkers alone insufficient for treatment decisions. For example, breast cancers with amplified HER2 expression frequently do not respond to the humanized monoclonal antibody trastuzumab (Herceptin). (4) Furthermore, initially responsive, receptor positive tumors may become refractory to targeted therapies over time, which occurs for HER2-amplified breast cancers (5) and many other types of cancer as well.

A common feature, and failure, of current biomarker approaches in breast and other cancers is their typically static, snapshot-in-time surrogate nature that does not directly evaluate tumor cell responses to particular agents for specific patients. A superior approach, if one was available, could be to rapidly determine by real-time monitoring how a tumor responds to a battery of candidate therapies and then to pick the agent(s) that are most efficacious for that particular patient's disease. Real-time mass profiling of living cells is a new and reproducible biophysical measurement modality that may provide a superior approach. Live cell mass

profiling is accomplished primarily using optical methods (6-9) or micro-fabricated sensors (10, 11) and can yield rapid, continuous quantification of single-cell dry mass changes in a population of cells exposed to a changing external environment, including the detection of cellular responses to growth-inhibiting or cytotoxic agents. (8) Unfortunately, due to technical limitations, live cell mass profiling has been constrained to cell types that exist as spatially-isolated single cells, such as bacteria, yeasts, and lymphocytes. This is a substantial roadblock to the effective use of mass profiling for solid tumor therapeutic response testing, such as in breast cancer. In general, dissected solid tumor samples even when mechanically disaggregated exist as a combination of small and large multi-cellular clumps, sheets, or spheres, rather than as purely single cells. Also, the agitation required to separate solid tumors into single cells may damage the cells and disrupts the cell-cell and cell-matrix interactions which may be crucial to maintenance of the malignant phenotype and required to assess agent responsiveness. (12, 13)

Using a mass profiling approach termed automated Live Cell Interferometry (LCI) we have overcome this inhibitory barrier. With LCI we profiled the therapeutic response kinetics of breast cancers that grow in culture as both single cells and as large colonies or clusters. These organized colonies were up to 50 cells in size and in principle much larger colonies could be accurately measured. We quantified the median growth rates of small populations of cells/colonies from four breast cancer cell lines exposed to trastuzumab over the course of six hours, which allowed us to rapidly differentiate Trastuzumab-sensitive from -resistant samples. In our study, LCI was performed without prior knowledge of which breast cancer lines expressed amplified HER2 surface receptor or at what level. Notably, LCI identified sensitive and resistant samples about a log-order more quickly than possible using traditional techniques, such as cell proliferation assays. This improvement in speed and sensitivity opens the way for

assessing sensitive versus refractory HER2-amplified breast cancer responses. It also provides a potential route for translation to the clinic, where often fragile, patient-derived cells are viable for short periods only and samples are most likely to be in the form of a heterogeneous mixture of single cells and aggregated clumps for many if not all solid tumor types.

Mass response profiling of four human breast cancer cell lines was performed over six hours using LCI with co-incubation of 20ug/ml clinical grade trastuzumab. For each cell type, a control well containing only culture media and a treated well containing trastuzumab were measured simultaneously. Two of the lines, BT-474 and SK-BR-3, have amplified HER2 with high level surface receptor expression and are differentially sensitive to trastuzumab in vitro as assessed by 5–7 day proliferation assays, whereas the other two lines, MCF-7 and MDA-MB-231, express the HER2 receptor at normal levels and are trastuzumab resistant. (16) Importantly, these cell lines grow with very different morphologies. MDA-MB-231 and SK-BR-3 lines grow as single-cells or in loose disaggregated clusters, whereas MCF-7 and BT-474 lines grow as dense multi-cellular colonies (**Fig. 3-1**). The relative scale between a single MCF-7 cell (mass ~5 x 10^2 pg) and a large colony (~22 x 103 pg) covers a 44-fold difference in mass (**Fig. 3-2**).

The masses of hundreds of individual cells and colonies were quantified continuously over 7h. Mean mass accumulation rates for each cell line at 30 min intervals were plotted to characterize the whole population response in the treated and control groups (**Fig. 3-3 a**). Treated and control samples of HER2 normal expression lines, MCF-7 and MDA-MB-231, exhibited an identical increase in mass over time. In contrast, the growth rates of treated and control samples for HER2 amplified high-expressing lines, BT-474 and SK-BR-3, began to diverge at ~4h of treatment. Trastuzumab sensitive lines, SK-BR-3 and BT-474, showed a highly

significant difference ($p < 0.001$) in growth rates whereas insensitive lines, MCF-7 and MDA-MB-231, showed no significant difference (**Fig. 3-3 b**). The BT-474 line was more responsive to trastuzumab than was the SK-BR-3 line, with control-to-treated mass fold changes of 0.0295 +/- 0.0065 and 0.0310 +/- 0.0090 respectively after 6h (mean +/- SEM; **Table 3-1**). Of the two sensitive lines, SK-BR-3 exists primarily as isolated single cells whereas BT-474 grows in small colonies, indicating that colony formation is not predictive or required for trastuzumab sensitivity or resistance. We also compared the LCI-measured response to trastuzumab to that determined with traditional multi-day, cell counting growth-inhibition assays. In all four cases, the trastuzumab sensitivity measured by LCI over 6h was concordant with that measured by cell counting over 3-7 days (**Table 3-1**).

These results show that live cell mass quantification via LCI can rapidly and sensitively detect the biologic response to trastuzumab in breast cancer regardless of the physical configuration or association of the cells being examined. Other recently-developed live cell mass profiling methods, such as MEMS micro-resonators, can measure the mass of single cells instantaneously with high accuracy, depending on the configuration of the micro-resonator. (10, 11) A drawback to this approach is that in order to achieve sufficient sensitivity, the active area of the resonator must be on the order of microns or smaller, which makes the continuous measurement of mixtures of single cells and larger multi-cellular colonies, as occurs for most solid tumor types, very difficult.

In general, quantitative phase optical microscopy approaches, including LCI, possesses mass measurement precision and accuracy on par with MEMS-based approaches, (6, 8) and their application to the study of cell clusters and clumps has been limited by practical difficulties

associated with high throughput phase imaging, rather than by fundamental physical limitations. Converting a raw phase image into mass information can be computationally challenging, particularly in the case of clusters of cells and objects with complex internal structures and optical thicknesses that are large compared to the illumination wavelength. (17) The increased speed of analysis and quantification of therapeutic responses for aggregated cell clumps, sheets, and spheres provides exciting new opportunities for agent selection and prognosis in solid tumor therapy.

Materials and Methods

Cell lines and Culture. BT-474, SK-BR-3, MDA-MB-231, and MCF-7 breast cancer cell lines were obtained from American Type Culture Collection (Rockville, MD). All lines were maintained in RPMI 1640 (Cellgro; Manassas, VA) growth media supplemented with 10% fetal bovine serum (Omega; Tarzana, CA) and 1% penicillin, streptomycin, and L-glutamine.

Drug Treatment. Clinical grade trastuzumab (Herceptin) (Genentech; South San Francisco, CA) was used at 20ug/ml.

Proliferation Assays. 5 x 10^4 cells were seeded into 12-well plates and allowed to adhere and grow for 2 days before beginning treatment. On days 0, 3, 5, and 7 of treatment with 20ug/ml Herceptin, cells were trypsinized and counted. To calculate the fold change, the doubling time was determined (DT = t*[log(2)/log(Nt/N0)]) for control and drug treated samples and the fold change taken as DTdrug/DTctrl. DT = doubling time, t = time, Nt = number of cells at time t, N0 = number of cells at time t = 0.

Confocal Fluorescent Imaging. Cells were seeded onto chambered coverglass and allowed to adhere overnight. Cells were fixed with 3.7% formaldehyde in 1 x PBS, pH 7.4, and permeablized in 0.1% Triton-X. Samples were then incubated with Alexa 568-Phalloidin actin stain (Invitrogen; Grand Island, NY) and DAPI. Confocal images were taken with a Zeiss LSM 780 CCD camera using Zen 2010 software.

Interferometer. The live cell interferometer has been described previously. (1-3) The system consists of a modified Bruker NT9300 optical profiler (Bruker; Tucson, AZ) with a 20X 0.28NA Michelson interference objective. The Michelson interferometer contains a beam splitter, reference mirror, and compensating fluid cell to account for the optical path differences induced by the fluid surrounding the sample. The phase shifting (PSI) method was used to capture phase images of the cell samples. To enable multi-sample imaging, LCI employs a small motor to adjust the interferometer reference mirror for small differences in cover glass optical path length at each sample well.

In our experiments, the assay time of ~6h was much shorter than the average time to division (24 hr+) and only a few cell divisions were observed per sample per run. However, in principle all of the cells tracked from time zero in the assay can be observed up to and through division, and their resulting daughter cells tracked in kind, allowing both total mass accumulation and total cell number to be measured in longer duration assays.

Data Analysis. Image analysis was performed using a custom, multi-step program written in Matlab (Mathworks Inc., Natick, MA). The first step was a phase-unwrapping step to remove

phase-errors (integer wavelength errors due to the ambiguity inherent in quantitative phase imaging) which remained after processing by the Goldstein phase unwrapping algorithm employed by Bruker Vision software (Bruker Nano Inc., Tuscon, AZ). This algorithm uses multiple random walks away from each pixel to remove integer wavelength jumps and non-physical excursions below background level. The second step is to segment each image into cell or colony objects using a combination of a local adaptive median filter and a watershed transform. Finally, objects identified by image segmentation were tracked using the particle tracking code adapted for Matlab by Daniel Blair and Eric Dufresne, based on the IDL particle tracking code developed by (2).

Cell Line	HER2 status	7 Day Doubling Time Tx vs. Ctrl +/− SEM	6 Hr Growth Inhibition Tx vs. Ctrl +/− SEM
MDA-MB-231	HER2 low	0.99 +/− 0.05 -fold	3.2 +/− 5.8%
MCF-7	HER2 low	1.13 +/−0.05 -fold	10.3 +/− 5.9%
SK-BR-3	HER2 high	1.45 +/− 0.06 -fold	18.5 +/− 5.4%
BT-474	HER2 high	5.55 +/− 0.99 -fold	39.0 +/− 8.5%

Table 3-1. Trastuzumab (Herceptin) sensitivity for four breast cancer cell lines as determined by a 7-day proliferation assay (column 3), and by growth inhibition measured by LCI at six hours (column 4). Growth inhibition at 6 hrs is defined as: (pct. growth Ctrl – pct. growth Tx) / pct. growth Ctrl. Calculation of doubling time is described and HER2 status was determined by O'Brien et al. [14]

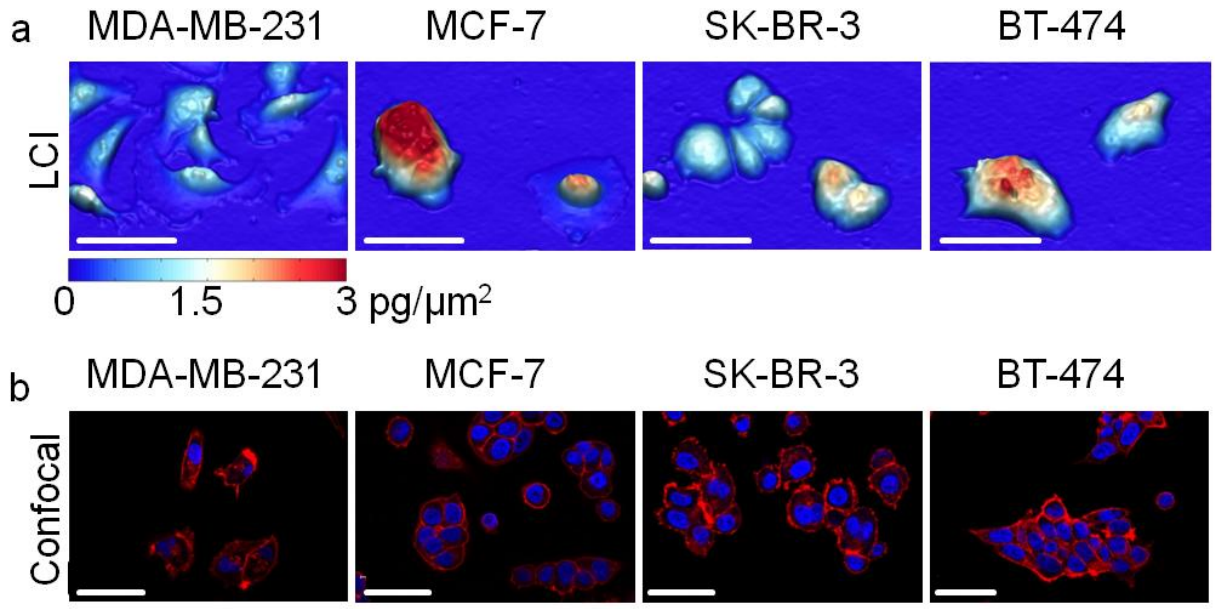

Figure 3-1. Single cells, cell clusters, and dense colonies can be imaged and mass quantified by LCI. (**a**) LCI phase images of mass distributions for each cell line. Single cells, loose clusters, and dense colonies are reproducibly quantified in real-time with LCI. Scale bars are 50um. (**b**) Confocal fluorescent images breast cancer cell lines. SK-BR-3 and MDA-MB-231 cell lines grow as single cells or in loose clusters, whereas the BT-474 and MCF-7 cell lines grow as dense multi-cellular colonies. Red is Alexa 568 Phalloidin actin stain and blue is a DAPI nuclear stain.

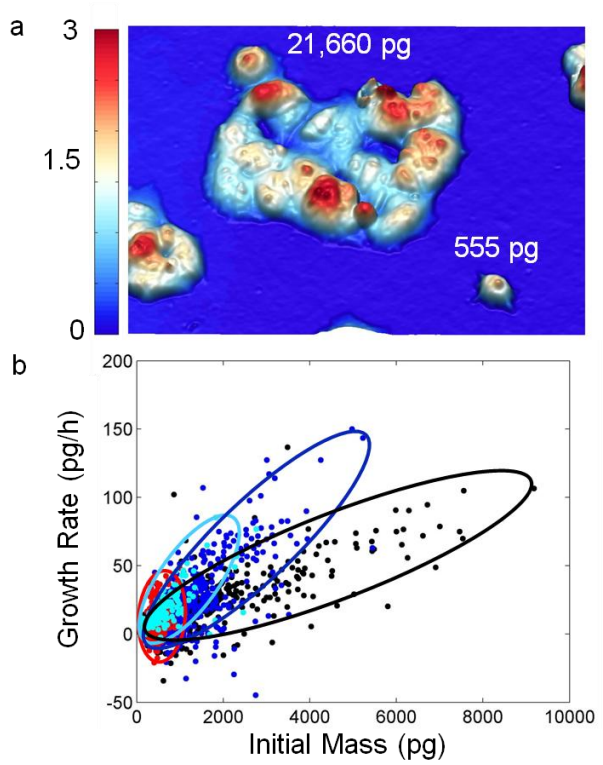

Figure 3-2. The LCI enables simultaneous imaging of single cells and large colonies. (**a**) The LCI phase image shows a single MCF-7 cell (555 pg) alongside a multi-cellular MCF-7 colony (21,660 pg) consisting of approximately 52 cells. Color scale denotes mass density in pg/um^2. (**b**) Composite scatter plot of growth rate vs. initial mass for all cell lines. MDA-MB-231 (red), MCF-7 (blue), SK-BR-3 (cyan), and BT-474 (black) are overlaid to show the range of cell and colony sizes and growth rates of the different lines. Colony forming lines (MCF-7 and BT-474) span the range from a single cell to large, multi-cellular colonies.

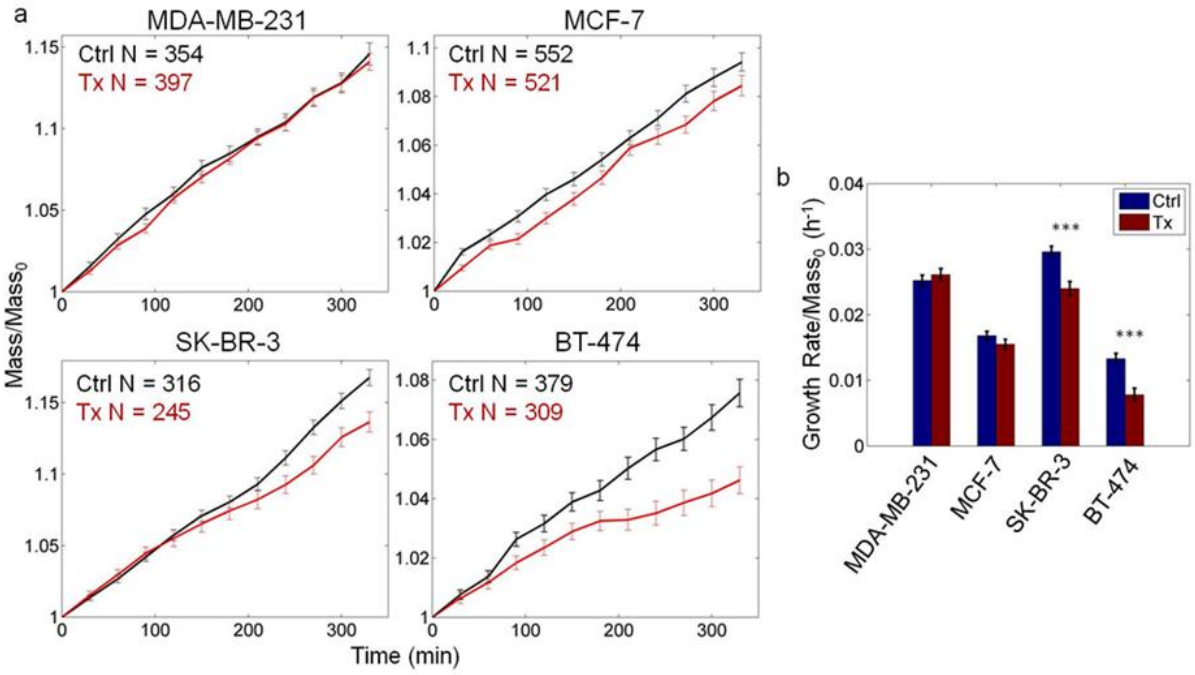

Figure 3-3. LCI reproducibly quantifies breast cancer cell growth inhibition due to trastuzumab within 3-5h. (**a**) Population mean normalized mass versus time plots for each cell line with 20ug/ml trastuzumab treatment (error bars indicate standard error). (**b**) Growth inhibition due to trastuzumab treatment becomes highly significant ($p < 0.001$) for the SK-BR-3 and BT-474 lines by 7h. Hourly growth rates are calculated from a linear fit to mass accumulation data.

References

1. R. Siegel, E. Ward, O. Brawley, A. Jemal. *CA Cancer J Clin*. 2011, **61** , 212-36.

2. M. Ignatiadis, C. Desmedt, C. Sotiriou, E. de Azambuja, M. Piccart. *Clin Cancer Res*. 2009, **15**,1848-52.

3. M. Ignatiadis, C. Sotiriou. *Nat Rev Clin Oncol*. 2012, **9**, 12-4.

4. JA. Wilken, NJ. Maihle. Primary trastuzumab resistance: new tricks for an old drug. In: Braaten D, editor. *Toward Personalized Medicine for Cancer 2010*. p. 53-65.

5. R. Nahta, FJ. Esteva. *Breast Cancer Research*. 2006, 8.

6. G. Popescu, Y. Park, N. Lue, C. Best-Popescu, L. Deflores, RR. Dasari, et al. *American Journal of Physiology-Cell Physiology*. 2008, **295**, C538-C44.

7. B. Rappaz, P. Marquet, E. Cuche, Y. Emery, C. Depeursinge, PJ. Magistretti. *Optics Express*. 2005, **13**, 9361-73.

8. J. Reed, J. Chun, T. Zangle, S. Kalim, J. Hong, S. Pefley, et al. *Biophys J*. 2011, **101**,1025-31.

9. J. Reed, J. Troke, J. Schmit, S. Han, MA. Teitell, JK. Gimzewski. *ACS Nano*. 2008, **2**, 841-6.

10. M. Godin, AK. Bryan, TP. Burg, K. Babcock, SR. Manalis. *Applied Physics Letters*. 2007;**91**.

11. K. Park, LJ. Millet, N. Kim, HA. Li, XZ. Jin, G. Popescu, et al. *Proc Natl Acad Sci U S A*. 2010, **107**, 20691-6.

12. BE. Miller, FR. Miller, GH. Heppner. *Cancer Res*. 1981, **41**, 4378-81.

13. MS. Wicha, G. Lowrie, E. Kohn, P. Bagavandoss, T. Mahn. *Proc Natl Acad Sci U S A*. 1982, **79**, 3213-7.

14. J. Reed, M. Frank, J. Troke, J. Schmit, S. Han, MA. Teitell, et al. *Nanotechnology*. 2008, **19**.

15. JC. Crocker, DG. Grier. *Journal of Colloid and Interface Science*. 1996, **179**, 298-310.

16. NA. O'Brien, BC. Browne, L. Chow, YH. Wang, C. Ginther, J. Arboleda, et al. *Molecular Cancer Therapeutics*. 2010, **9**, 1489-502.

17. D. Ghiglia, M. Pritt. *Two-Dimensional Phase Unwrapping: Theory, Algorithms, and Software*: John Wiley & Sons; 1998

CHAPTER 4

Quantification of biomass and cell motion in human pluripotent stem cell colonies

Human pluripotent stem cells (hPSCs) generate all embryonic cell types and can be grown for prolonged periods in culture, with their pluripotency/self-renewal program controlled by chromatin structure and a core transcription factor network (1). hPSCs are also small, replicate rapidly, and grow in tight colonies. It remains unknown whether the size and growth rate of hPSCs are regulated by the program that regulates pluripotency/self-renewal, a question that has important implications for our understanding of the relationship between growth rate controls and early differentiation. Interestingly, key features of hPSCs can be re-established in somatic cells by reprogramming factors (2) and recent, single-cell imaging studies have shown that fibroblasts reprogrammed to hPSCs undergo an increase in proliferation and reduction in area/size within the first cell division (3). This work identified replicative and size barriers that must be rapidly overcome for successful reprogramming. Reprogramming to and differentiating from pluripotency are overtly similar but opposite processes (4), and it is unclear whether analogous barriers or checkpoints also exist early during hPSC differentiation. Unfortunately, the growth of hPSCs in tight, multi-cellular clumps has blocked direct, in-situ measurements of cell growth, size, and other fundamental properties, such as intra-colony motion during early hPSC differentiation. It therefore remains uncertain whether hPSCs undergo a decrease in proliferation and increase in size with induced differentiation, or whether changes in cell proliferation and size (biomass) are coordinated with early hPSC differentiation programs (5).

To date, hPSC size measurements have been imprecise and used to document extreme changes in cross-sectional area by microscopy (3). hPSC growth is typically measured as time to division

and not as changes in cell biomass, which is the most direct measure of net cellular growth but requires detection at <5% mass change per hour. Existing optical approaches have also revealed that individual PSC colonies are highly motile, a property which may skew clonogenic counting assays through colony merging (6). Coordinated cell movement within hPSC colonies could provide a basis for colony migration and merging, although this too remains unknown for hPSCs grown in culture (6-8).

In general, cell size has been inferred from the radius or projected area for cells with fixed geometries, such as bacteria, yeasts, and spherical lymphocytes. However, most animal cells, or cells that grow in colonies, have irregular and often changing shapes, resulting in poor estimates of cell biomass based on measurements of projected area (**Fig. 4-S1** in the Supporting Material). Additionally, changes in cell volume or area may result from changes in solute concentrations or flattening against a substrate rather than from changes in biomass. Flow cytometry measures material density gradients and aqueous content to estimate cell size, but cannot quantify the continuous growth of hPSC colonies (9). More promising are MEMS micro-resonators, which can accurately measure the mass of single cells instantaneously and over time (10, 11). However, for sufficient sensitivity a resonator must be microns or smaller, making continuous measurements of motile, growing hPSC colonies practically impossible.

To provide an approach for addressing fundamental questions regarding mass and growth control in hPSCs and during early differentiation, we evaluated live cell interferometry (LCI) as a method for quantifying mass distributions within HSF1 hPSC colonies over time. LCI takes advantage of the fact that as light passes through a transparent object, such as a cell, it slows down due to the interaction of light with matter (12, 13). This retardation of light due to the

interaction with cellular biomass causes a phase shift relative to unperturbed light which is measured using a Michelson interferometer (13). Assuming a cellular average for the relationship between density and changes in refractive index, the measured phase shift at each location inside of the cell is directly proportional to the amount of biomass at that location, resulting in a map of the distribution of mass for all non-aqueous components (dry mass) (12-15). In this study, we assume that the conversion factor between phase shift and mass, the inverse of the specific refractive index, is 5.56 pg/μm^3, although we note that this parameter only varies by about +/- 10% among the typical contents of a cell (12, 13). Assuming the average contents of the cell/colony remain fairly constant over the measurement period, the specific value of this parameter will drop out of any measurements based on relative mass comparisons, such as the specific growth rate. Recent applications of quantitative phase microscopy using other imaging platforms include measurements of cell growth (14), cell death (16), membrane mechanics (17), individual organelles (18), and preliminary imaging of mouse PSCs (19). Prior work with LCI establishes it as a method for repeatable (<2% CV) quantification of mass, mass accumulation rate, and mass distributions for large populations of cells on a single cell basis (13, 20), but not for cells constrained within hPSC colonies.

Materials and Methods

Cell line and growth media. HSF1 human embryonic stem cells (hESCs; 46XY; UC-0001) were grown on feeder-free Matrigel (BD Biosciences) in defined cell culture media (Invitrogen StemPro SFM) with daily media changes, as described previously (21, 22). Differentiation with RA was induced by replacing bFGF with 10 μM RA (Acros Organics).

Cell Counting. Cell counting was performed using a Neubauer hemocytometer after trypan blue staining (Invitrogen).

EB Formation Assay. Embryoid body (EB) formation was performed as described previously (21). Briefly, hESCs were trypsinized to single cells and 106 cells were placed in one well of a AggreWell 400 plate (Stemcell Technologies) according to the manufacturer's instructions. The next day, EBs were harvested and grown in IMDM medium supplemented with 20% FBS for 10 d in a Corning Costar Ultra-low attachment 6 well plate (Sigma-Aldrich). Media was exchanged every 2-3 d. An inverted light microscope was used to assess and count EBs.

Gene Expression Profiling. Total RNA was extracted from control or RA-exposed hESCs using Trizol reagent (Invitrogen) according to the manufacturer's instructions. cDNA was synthesized from total RNA using a Superscript III first-strand cDNA synthesis kit (Invitrogen). Real-time PCR was performed with a SYBR Green PCR kit (Diagenode) with denaturation at 94 °C for 15 s, annealing at 60 °C for 30 s, and extension at 72 °C for 45 s over 40 cycles. Primer sequences are available upon request.

Cell Cycle Analysis. Cells were harvested by trypsinization, then stained for DNA content with propidium iodide (Sigma). Single color flow cytometry was performed on a BD Accuri C6 flow cytometer (BD Biosciences) and data collected for 30,000 to 150,000 events. Cell cycle analysis was performed in FlowJo (Tree Star Inc.) using a Dean-Jett-Fox model fit to the propidium iodide fluorescence intensity histogram.

LCI Imaging. LCI imaging was performed on a Contour GT-X8 optical profiler with a through transmissive media (TTM) attachment (Bruker). Cell viability was maintained using a custom live cell flow chamber (13, 20). 20mm x 20mm square silicon substrates were treated with SigmaCote (Sigma) and 1 M NaOH prior to coating with Matrigel to obtain a surface suitable for hPSC growth (23). HSF1 cells plated as small colonies onto treated silicon were imaged 1, 5, or 7 d after plating (0, 4, or 6 d after the start of RA exposure). Cells were viable with no visible defects in morphology after over 12 h on the interferometer stage under constant illumination. Most colonies were imaged for 2 h at 11x effective magnification. Because of the difficulty in finding colonies which were large, but that did not extend outside of the microscope observation area, most colony growth rate measurements focus on colonies that spanned at most one or two individual microscope fields of view. A subset of experiments were performed using a large grid of 12x15 images with 50 μm overlap between edges for stitching (as in **Fig. 4-2 A**). To obtain unaliased estimates of the rate of mass motion, representative smaller colonies were measured at 20x magnification with 30s between images (Fig. **4-6 A-F** and **Fig. 4-S7 A-F**).

Statistical Analysis. Statistical analysis was performed using a two-tailed Student's T test with unequal variances and sample sizes (Welch's T test). Error bars are reported as +/- standard error (SE).

Image Analysis. All image processing was performed using custom Matlab (Mathworks) scripts, as described below.

Phase Unwrapping. Phase errors, integer wavelength errors caused by a one-wavelength ambiguity inherent in quantitative phase imaging (24), were corrected using a random walk-based algorithm which removes integer wavelength jumps and excursions below the background level.

Stitching. Images were stitched together using an optimization algorithm implemented in Matlab that adjusts the offset and planar tilt of each frame in order to minimize the sum of the differences between the overlapping regions of each adjacent image.

Total Colony Mass, Mass Accumulation Rate, and Area. Colonies were located by local adaptive thresholding based on Otsu's method (25), and then the mass distributions within these pixels were summed to obtain colony total mass. The slope of a least squares best fit line to total mass versus time is the colony mass accumulation rate. Errors in this value are estimated as the standard deviation of the mean slope (26). Colonies with errors exceeding the estimated growth rate were excluded from the reported average growth rates. Average growth rates including these estimated error rates were determined using a Monte Carlo routine with 10,000 samples, implemented in Matlab and run twice with different pseudo-random number seeds and compared to check convergence. For each sample in the Monte Carlo simulation, the empirical cumulative density function of the log-transformed specific growth rate data was fit to a Gaussian cumulative density function to estimate the population mean and standard deviation (**Fig 4-S3 A**). The average and standard deviation of these estimated values over all trials is the reported mean growth rate. Additional results from this analysis are presented in the supporting information (**Fig. 4-S3 B**). Colony area is estimated based on the area of the region determined by Otsu thresholding.

Growth Rate Versus Mass Curve Fitting. Growth rate versus mass data were fit in Matlab using the Curve Fit toolbox with a nonlinear least squares fit with an unconstrained trust region algorithm, weighted by the square of the standard error of the growth rate measurements. Confidence intervals on the power law scaling exponent are based on the Student t test at a significance level (two-tailed) of p = 0.05.

Local Mass Accumulation Rate. To measure mass accumulation rate distributions within individual colonies, as in **Fig. 4-3**, we first remove translational motion by aligning successive colony images based on cross-correlations between frames. We then use Otsu's method (25) on the location-shifted, time-averaged image to find pixel locations of highest average intensity. This yields a measure of mass versus time m(x,y,t) at each pixel location, x, y. We perform a least squares fit on the m(t) measurement at each pixel within the colony and estimate the local mass accumulation rate as the slope of this best fit line. Finally, we use a Gaussian low-pass filter with a spatial standard deviation of 10 μm to smooth out high spatial frequency variations while maintaining adequate colony-scale resolution.

Decorrelation Timescale. To find the decorrelation timescale, we first estimate the autocorrelation, C_{XX}(27), at every time shift, Δt, by applying a sliding window of width w discrete time steps:

$$C_{XX}\left(x,y,t_0,\tau,\Delta t\right) \approx \sum_{i=1}^{w} m(x,y,t_0+i\cdot\Delta t)\cdot m(x,y,t_0+\tau+i\cdot\Delta t)$$

where we use w = 20 (10 minutes at 30s per image) to get adequate resolution of the typical timescales with minimized computational cost. We then average this function C_{XX} across all pixel locations x y, all starting at time t_0, and all time shifts, τ, to get an overall averaged

autocorrelation $C_{xx}(\Delta t)$ (**Fig. 4-S8**). Finally, we apply a linear least squares fit to this function, $C_{xx}(\Delta t)$, and find the slope of this best fit line. This slope is an estimate of the decorrelation rate, or how quickly the mass distribution within the colony is changing over time.

Average Cell Mass. The mass of individual cells within colonies was measured with LCI, then, while on the microscope stage, colonies were fixed with paraformaldehyde (Sigma), permeabalized in a solution of Triton-X (Sigma), and stained with a fluorescent nuclear stain (YOYO-1, Invitrogen). Cell number was determined by manual counting the number of cells within each colony after processing with a custom Matlab script (**Fig. 4-S5**). Average mass per cell was computed as the total colony mass divided by the number of cells.

Coordination Distance. For each stack of colony images, we first identify the colony using Otsu thresholding (25) on a composite mean image of all frames. Then, for each pixel within the colony, we compare the local rate of mass increase at each location to the average colony growth rate to generate a binary image where each pixel indicates either sign of mass accumulation relative to the mean as either positive (green in **Fig. 4-6 A** and **D**) or negative (red in **Fig. 4-6 A** and **D**). At each pixel in this binary image, we estimate $P(\Delta x)$ as the (sum of all pixels within Δx +/- 0.5 μm that agree with the sign of mass increase)/(total number of pixels within Δx +/- 0.5 μm), where Δx is the Euclidian displacement from the current pixel. Finally, we average the $P(\Delta x)$ profile estimates from each pixel within each colony in the sample to get the final, empirical $P(\Delta x)$ profile (such that, for example, the $P(\Delta x)$ for day 0 control represents the average of over 7×10^6 pixel-wise estimates of $P(\Delta x)$). Here, we approximate $P(\Delta x)$ as an exponential decay and define the coordination distance as the exponential decay constant of $P(\Delta x)$.

Results

We quantified the biomass of a total of 728 HSF1 colonies at 1, 5 and 7 d timepoints using LCI (Fig. 1 and Fig. S1). LCI provides precise and reproducible biomass measurements for both small and large hPSC colonies over a range of 6 orders of magnitude, from subcellular fragments of ~10 pg to the largest colonies spanning multiple image frames with masses up to ~10 µg (**Fig. 4-2 A**). The mass of individual colonies was tracked over a period of 2 h at selected timepoints from the first several days in culture, enabling studies of hPSCs and the earliest stages of differentiation (**Fig. 4-2 B** and **C**). LCI quantifies hPSC growth rates within 2 h, which is

significantly faster than conventional cell proliferation rate measurements (2-6 d). These measurements are robust to changes in colony morphology and mass distribution observed with LCI (**Fig. 4-S6** and **4-S8 D**).

LCI data show a consistent, exponential rate of hPSC colony mass accumulation under standard self-renewing growth conditions regardless of starting colony mass (**Fig. 4-3 A** and **Fig. 4-S2**). This result was confirmed by a moderate relationship between colony mass and mass accumulation rate (R^2 = 0.87) and a linear power law dependence (power law scaling exponent = 1.05 +/-0.025 at 95% confidence). For large colonies, this relationship is expected independent of the mass trend for individual cells (e.g., linear or exponential increase of mass with time) provided that the mass accumulation rate of each cell is not affected by colony size (Supporting Analysis). These data therefore indicate that hPSC colony size does not affect the mass accumulation rate of individual cells within a colony under normal growing conditions either from positive or negative influences.

The observed exponential increase of colony mass is governed by a single parameter, the specific growth rate = $(dm/dt)/m$ (growth rate normalized by mass). We fit the distribution of measured specific growth rate for 658 HSF1 colonies to a log-normal distribution and obtained a mean specific growth rate of 0.03 h^{-1}, with a standard deviation of 0.63 ln(hr^{-1}) (**Fig. 4-3 B** and **Fig. 4-S3 A** and **B**). This value corresponds to a mass doubling time of 22.8+/- 1.1 h (**Fig 3 C**). Cell counting yielded a mean cell number doubling time of 24.9 +/- 1.2 h (**Fig. 4-3 C** and **Fig. 4-S3 C**). This result is not significantly different from our population average mass accumulation rate, although we note that cell counting is intrinsically a bulk measurement and does not reveal the trend of colony growth rate with increasing colony size and typically requires an experiment duration of several doubling times. Using LCI, we were able to make growth rate measurements at multiple distinct timepoints in the 7d total experiment duration, which showed that there was also no significant variation of the mean specific growth rate with time since last passage, despite dramatic differences in colony size (**Fig. 4-S3 D**). Additionally, there were no significant differences in mean specific growth rate or the power law scaling exponent of the growth rate versus mass data when only the smallest colonies were considered in the analysis (**Fig. 4-S3 E** and **F**).

We induced tri-lineage differentiation by HSF1 exposure to 10 μM retinoic acid (RA) starting at 24 h after plating (0 d) to serve as a model of early induced differentiation. Cell cycle analysis showed a substantial increase in the G0/G1 subpopulation (**Fig. 4-4 A** and **Fig. 4-S4 B** and **C**) and gene expression profiling showed loss of *OCT4* and induction of homeobox family and tri-lineage differentiation genes *MSX2*, *GATA3*, and *HAND1* by 4 d of RA exposure (**Fig. 4-4 B** and **Fig. 4-S4 A**). Morphological changes were also consistent with RA-induced differentiation (**Fig.**

4-5 A). Colonies were imaged with LCI after 4 and 6 d of continuous RA treatment and mass accumulation rates measured, as for untreated colonies (**Fig. 4-3 A** and **Fig. 4-S3 B** and **D**). Surprisingly, a decrease of ~15% in the rate of mass accumulation occurs during RA-induced differentiation (**Fig. 4-3 C**), despite the appearance of cells with significantly larger projected areas (**Fig. 4-5 A**). The magnitude of this change cannot be explained by the moderate, 3-percentage point increase in the fraction of dead cells observed during RA differentiation (**Fig. 4-S4 D**). This result contrasts sharply with the almost immediate reduction in cell size and nearly 50% increase in proliferation rate observed at the earliest stages of successful reprogramming to pluripotency (3) and the 100% decrease in proliferation rate typically observed in the differentiation of murine ESCs (5). These results indicate that the net hPSC growth rate before and during early differentiation is maintained independently of programs that regulate self-renewal or early differentiation.

HSF1 cells appear small, but their native size in colonies has not been accurately measured (5). An increase in HSF1 cell area is associated with a transition to fibroblast-like appearing cells during induced tri-lineage differentiation (**Fig. 4-5 A**). However, this increase in area is accompanied by a significant decrease in projected mass per area (**Fig. 4-5 B**), which is consistent with the near constant growth rate (biomass accumulation) during this transition. LCI was used in combination with fluorescent nucleus staining to measure the average mass per cell within intact colonies (**Fig. 4-5 C** and **D** and **Fig. 4-S5 A** and **B**). We also characterized the relationship between average cell mass and the average distance between daughter cells (**Fig. 4-S5 C**). As colonies differentiate the distance between individual cells increases (**Fig. 4-S5 C** and **Fig. 4-S8 B**). We observe no statistically significant relationship between cell mass and distance between adjacent cells, further supporting the conclusion that average mass per cell is

approximately constant during early differentiation, across all observed colony morphologies (**Fig 4-S5 D-G**). Despite large changes in the HSF1 gene expression program (**Fig. 4-4 B** and **Fig. 4-S4 A**) and a previously reported shift from glycolysis to oxidative phosphorylation (21), no significant differences arise between the average mass per cell in pluripotent colonies versus colonies differentiated for 4 d with RA exposure. Cell doubling time is minimally affected (**Fig. 4-3 C**), but the proportion of cells in G0/G1 phase of the cell cycle increases substantially (**Fig. 4-4 A** and **Fig. 4-S4 B**), preceding changes in proliferation or growth rate (**Fig. 4-3**) and cell size (**Fig. 4-5**).

LCI quantification reveals where mass is increasing or decreasing within colonies and how quickly the mass distribution changes over time (**Movies S1-S4**). In order to quantify changing mass distributions over time we imaged selected colonies at a higher data rate and magnification (30s between each frame, 20x effective magnification, 40 min total observation time). Representative images showing local mass accumulation and loss rates overlaid on colony images show much larger areas of coordinated mass change in HSF1 colonies than in RA-differentiated colonies (**Fig. 4-6 A** and **D** and **Fig. 4-S7 A-F**). The local mass accumulation and loss rates shown in these images represent the sum of local biomass production and destruction, as well as reorganization in the mass of individual cells and the motion of individual cells within colonies. However, due to the relatively short imaging period, in which the total biomass accumulation is only approximately 1% of the colony total mass, these images primarily represent the redistribution of mass within colonies, rather than the creation or destruction of biomass. The pattern of mass redistribution shown in **Fig. 4-6 A** appears as a stretching of the colony along the horizontal axis with a resulting contraction along the vertical axis, which was not observed in RA-treated colonies (**Fig. 4-6 D** and **Fig. 4-S7 D-F**).

The autocorrelation function is useful in biological image analysis to quantify the persistence of deviations from the average (28). We measured the decay rate of the autocorrelation of mass versus time for all 2 h colony mass distribution measurements to determine the persistence of fluctuations in intra-colony mass distributions. This rate gives an indication of how quickly mass is being reorganized within individual colonies as a result of both mass transport within individual cells as well as motion of cells relative to one another. The decorrelation rate of undifferentiated and RA-differentiated colonies shows a significantly lower ($p < 10^{-5}$) value for differentiated colonies, consistent with a much slower reorganization of cellular mass within these colonies as compared to untreated HSF1 colonies (**Fig. 4-7 A**).

The regions of local mass increase or decrease in pluripotent colonies are substantially larger than the regions of mass increase or decrease in RA-differentiated colonies (**Fig. 4-6 A** and **D** and **Fig. 4-S7 A-F**). To quantify this appearance, we analyzed the distributions of local mass increase and decrease by measuring the frequency with which two locations within a colony were either both increasing or both decreasing in mass as a function of displacement within the colony, defined here as $P(\Delta x)$. This quantity, $P(\Delta x)$, should be equal to 1.0 at very short distances

(meaning adjacent locations are highly likely to increase or decrease in mass together), and should fall to 0.5 at large distances (because when two locations are very far from one another, by random chance they will both happen to be rising or falling together about 50% of the time). The rate of decay of this probability from 1.0 to 0.5 with displacement indicates the degree of coordination of mass motion within colonies, with more coordinated colonies showing a slower rate of decay. Pluripotent colonies measured up to 6 d in culture show a significantly slower

decrease in P(Δx) and a significantly larger coordination distance than RA-differentiated colonies, characteristics which are lost during the first 1-2 d of RA exposure (1080 total colonies, **Fig. 4-7 B** and **C** and **Fig. 4-S8 A**). The distance over which coordination decays in RA-treated colonies is approximately the distance between neighboring cells, whereas untreated colonies show coordination up to approximately two cells away (**Fig. 4-7 B** and **Fig. 4-S8 B**). These data reveal that coordinated cell movements, detected as shifts in colony mass distributions, occur in hPSCs and stop early during RA-induced differentiation.

Discussion

Cells appear to get larger and grow more slowly early during hPSC differentiation (5). However, our results using a HSF1 model of early induced differentiation show that transitions in gene expression, colony morphology, and cell cycle phase durations during early differentiation (29) occur with a nearly constant cell mass and rate of mass accumulation (**Fig. 4-3 C** and **Fig. 4-5 C**). Additionally, this flat or slightly negative growth rate change occurs in early HSF1 differentiation during the transition from glycolytic to oxidative energy metabolism (21). Although the more glycolytic metabolism of hPSCs, reminiscent of the Warburg effect in cancer, may support a slightly higher growth rate (30), its impact on cell mass appears minimal. This is particularly striking in light of cell volume measurements (5), which have shown an increase in cell size during differentiation. This suggests that during early differentiation, cell mass is perhaps regulated independently of cell volume, giving rise to a change in cellular density, as has been observed in recent measurements of the mass and volume of budding yeast (31). This should be investigated further in future work.

hPSCs in vitro show coordinated mass redistribution/intra-colony cell movement, which is

reminiscent of, but not identical to, cell patterning in early embryonic development (7, 8). The loss of motion coordination after RA treatment suggests that these programs are silenced during early hPSC differentiation, in contrast to the program that regulates cell size/biomass, which is maintained. Cytoskeletal components, including the Rho-associated kinase, and adhesion molecules, such as E-cadherin, regulate asymmetric hPSC colony growth, inter-colony movement, and colony fusion events (6) and may play a role in this observed coordination. The label-free and quantitative nature of the LCI technique means it can be used to track the motion of all biomass, rather than specific, labeled features or edges, in a consistent way from single cells to entire colonies. This method may therefore have utility in studying the impact of cell mass redistribution in other models of hPSC differentiation, beginning with the earliest specifying events.

Spatial autocorrelations of quantitative phase images have previously been used to assess the mechanical properties of red blood cells (RBCs) undergoing morphological changes (32). In the RBC case, the relatively simple cell composition and single cell dispersion allows for derivation of a direct relationship between quantitative phase data and cellular mechanical properties. In particular, at low frequencies, Park et al.(32) note a moderate anticorrelation in the spatial phase thickness autocorrelation, which is suppressed with increasing RBC stiffness. We note the presence of a similar anticorrelation in the LCI $P(\Delta x)$ parameter for control colony measurements on days 0 and 4.

Overall, our results show that large changes in HSF1 colony morphology and motion occur during early RA-induced differentiation, preceding any potentially large shifts in cell size and growth rate during later stages of lineage-specific differentiation. Revealing these features using

a novel LCI approach improves our understanding of early hPSC differentiation, which may have practical importance for using differentiated hPSCs in regenerative therapies.

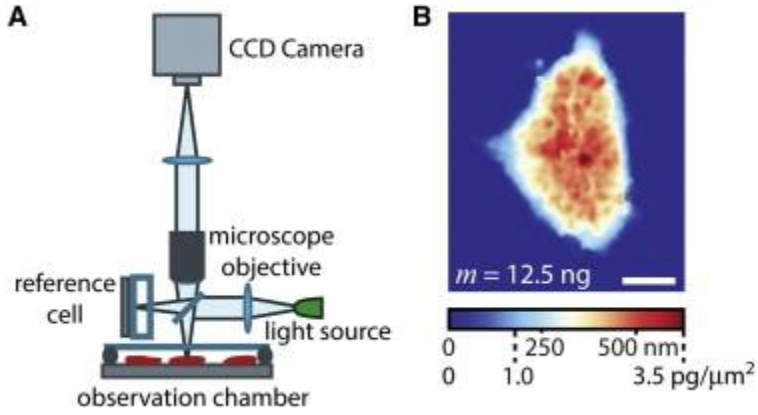

Figure 4-1. LCI quantifies HSF1 hPSC colony mass. (**A**) Simplified schematic of the live cell interferometer (LCI) used to obtain dynamic mass distributions of living cells. LCI uses a standard light microscope with a Michelson interferometer between the microscope objective and the temperature and CO^2 controlled observation chamber. The interferometer compares lights which passes through cells to light which passes undisturbed through a reference chamber. (**B**) LCI directly measures the phase shift of light due to its interaction with the material inside a cell. This is converted to cell dry mass using the measured relationship between light phase shift and material density, yielding the mass distribution within each individual colony. Scale bar in (B) is 20 µm.

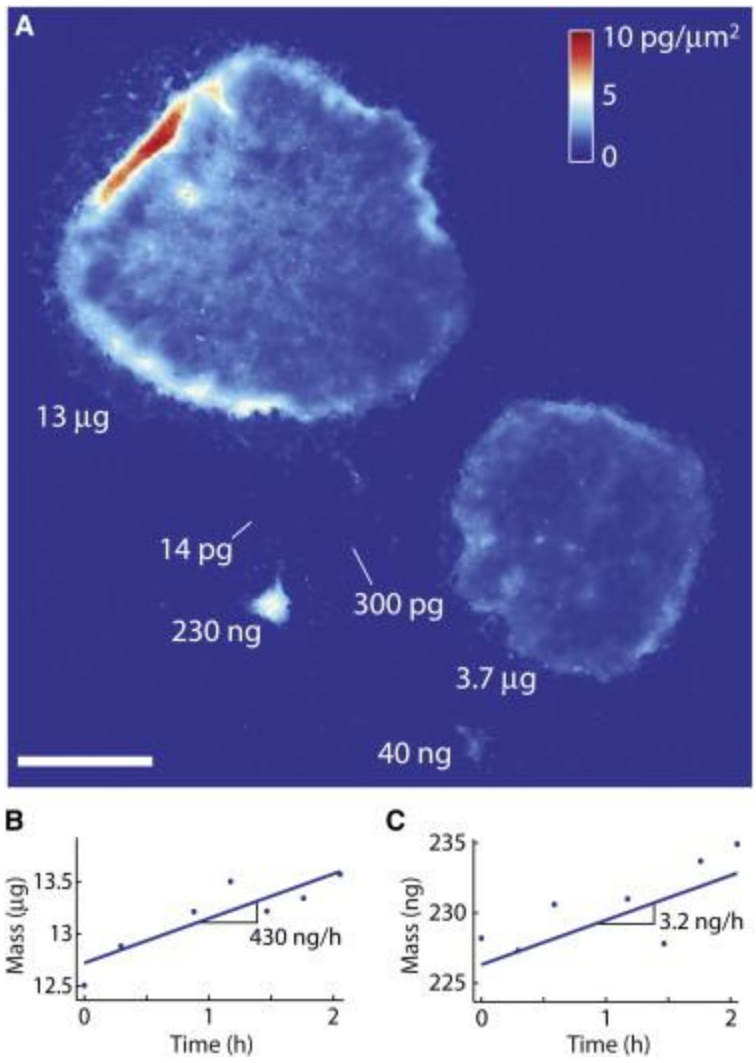

Figure 4-2. LCI quantifies hPSC colony mass accumulation rates for undifferentiated HSF1 cell clusters spanning 5 orders of magnitude in mass. (**A**) Stitched LCI image of HSF1 colonies after 7 d in culture showing mass measurements spanning a dynamic range of 6 orders of magnitude. The largest visible colony has a total mass of 13.5 µg, whereas the smallest visible cellular fragment has a mass of 14 pg. (**B,C**) Mass versus time plots of two colonies from part (A). Scale bar in (A) is 1 mm.

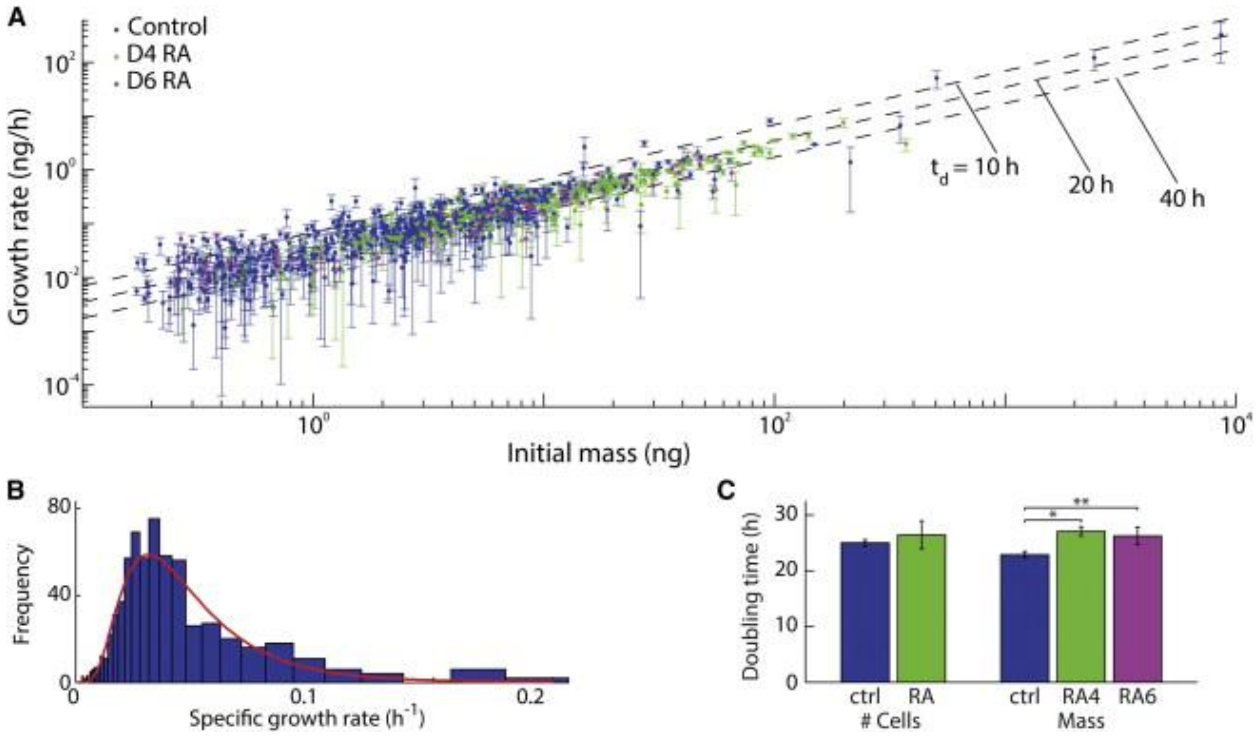

Figure 4-3. Average mass accumulation rate for untreated and retinoic acid (RA)-exposed hPSC colonies. (**A**) Growth rate versus initial mass for untreated and RA-exposed hPSC colonies shows an exponential growth rate for mass accumulation across 5 orders of magnitude in mass. RA treated colonies show similar mass accumulation rates to untreated colonies. Error bars show the uncertainty in measured growth rate calculated as the standard deviation of the slope of the biomass versus time measurements. Error bars appear uneven due to the logarithmic scale. (**B**) Histogram of untreated control colony growth rate measurements (normalized by initial mass to provide specific growth rate) with the log-normal curve (red) showing the estimated distribution of specific growth rates that was used to compute doubling time. (**C**) Doubling time from cell counting is unable to distinguish cell proliferation rates between control and RA exposed hPSCs during 4 to 6 d of growth. Doubling time for cell mass shows a decrease of approximately 15% with RA treatment (based on measurements of 658 ctrl, 227 RA d 4, and 62 RA d 6 colonies). ctrl = control, RA4 = 4 d of RA treatment, RA6 = 6 d of RA treatment. Error bars show +/- SE *$p < 0.05$, ** $p<0.001$.

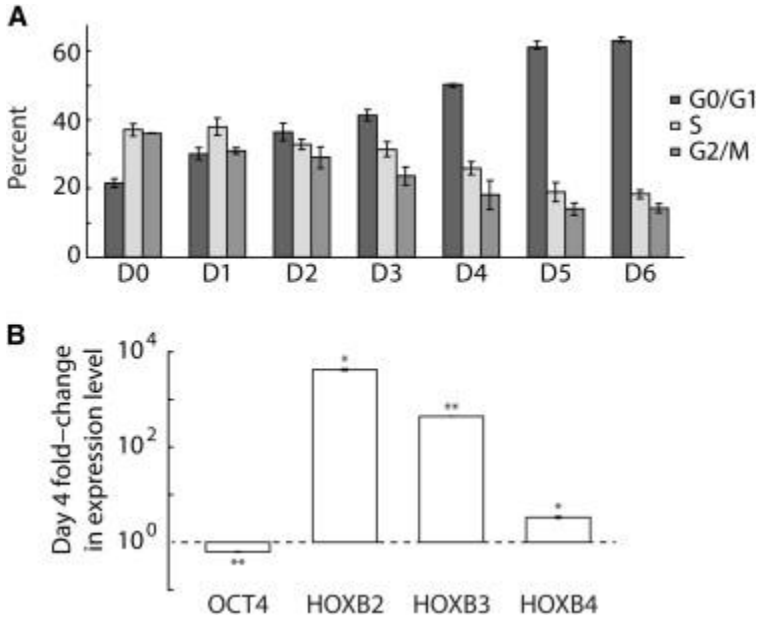

Figure 4-4. Cell cycle and gene expression profiling of RA-exposed HSF1 hPSC colonies. (**A**) Cell cycle analysis of RA-treated colonies shows a substantial increase in G0/G1 fraction, and decrease in S and G2/M fractions by 4 d of RA treatment. (**B**) Gene expression after 4 d of RA treatment shows induction of homeobox family genes and loss of pluripotency marker OCT4. Error bars show +/- SE. *p < 0.05. **p < 0.01.

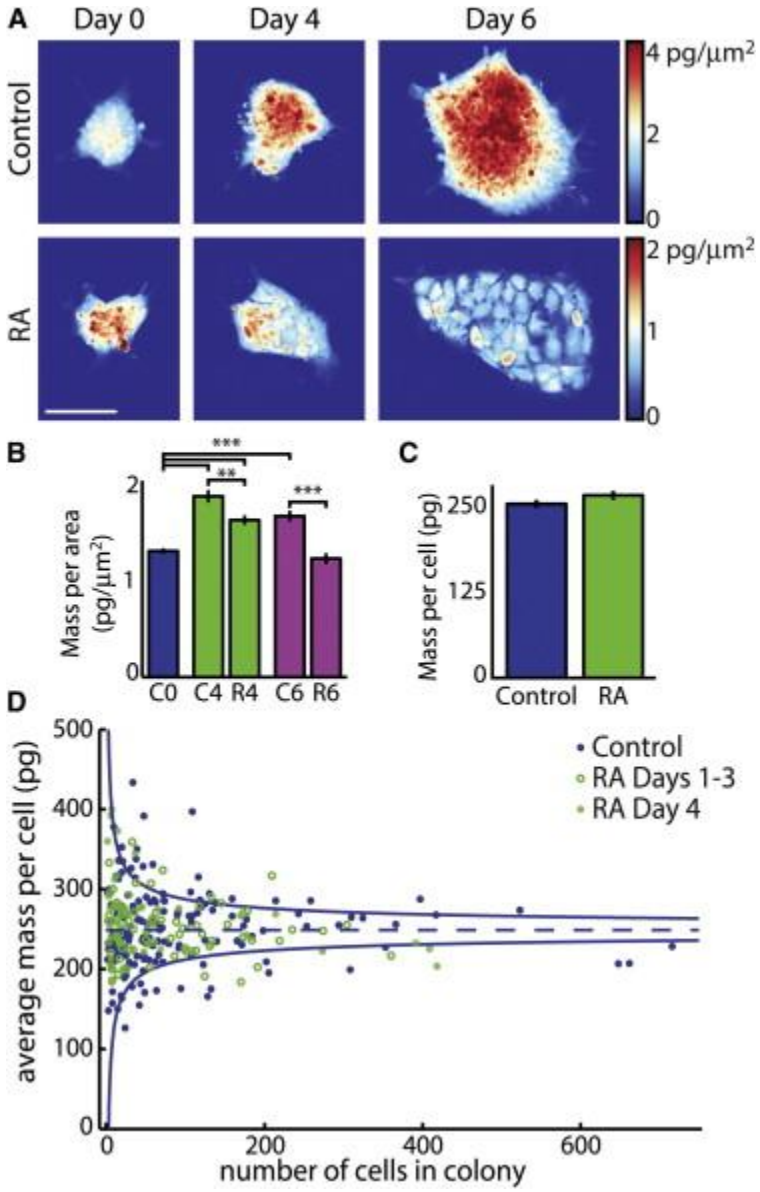

Figure 4-5. RA-differentiated hPSCs have a lower density, but the same total mass, as pluripotent hPSCs. (**A**) Colonies showing morphological changes associated with RA-induced differentiation. RA-treated cells visible within colonies have a lower mass per area (note color bar) but much larger area. (**B**) Comparison of mass per area (density) of hPSC colonies with and without RA treatment. (**C**) Comparison of average single cell mass shows no significant change in mass per cell during differentiation. (**D**) Plot of all average single cell masses from untreated and RA-treated colonies. Solid blue lines show the mean +/ s.d. of the control

measurements (μ = 250 pg) assuming $\sigma = \sigma_{OneCell}\, n^{-1/2}$as expected for the population standard deviation. Scale bar in (A) is 100 μm. Error bars show +/- SE. ** $p<0.001$, *** $p<10^{-6}$.

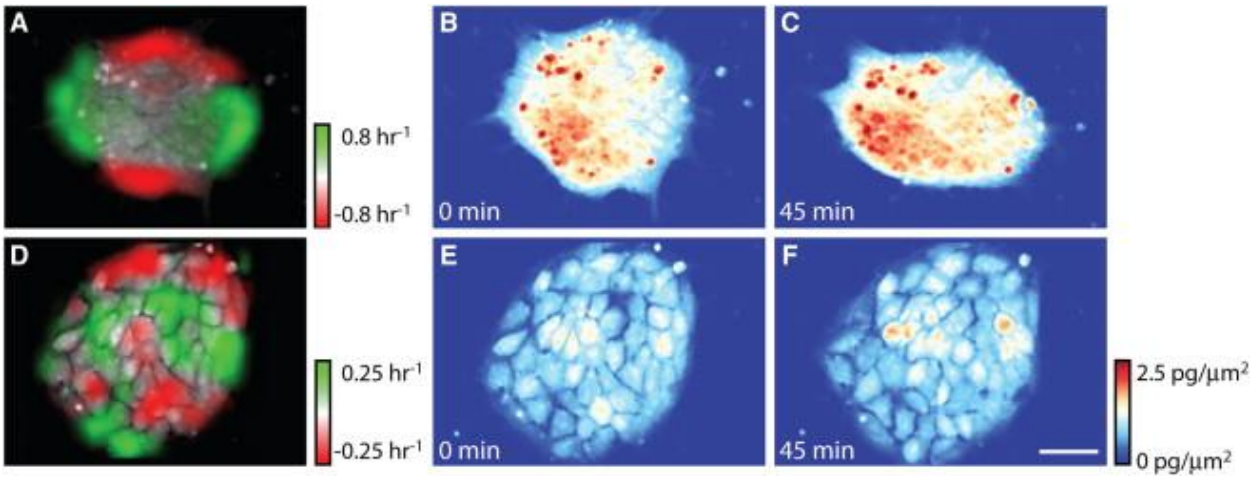

Figure 4-6. HSF1 hPSCs exhibit larger, faster areas of mass redistribution within colonies, indicating a higher degree of movement coordination, than RA-exposed hPSCs. (**A,D**) Maps of local specific growth rate (change in mass normalized by average mass) over 45 min for representative (**A**) undifferentiated and (**D**) RA-differentiated hPSC colonies (green = mass accumulation; red = mass loss). The pattern of mass redistribution in (**A**) shows a large change in undifferentiated colony morphology (stretching) along the horizontal axis (**B,C**) and the generally larger change in mass distribution in undifferentiated versus differentiated colonies. RA-differentiated colonies show a much smaller mass re-distribution and little change in overall colony morphology (**D-F**). Scale bar is 50 µm.

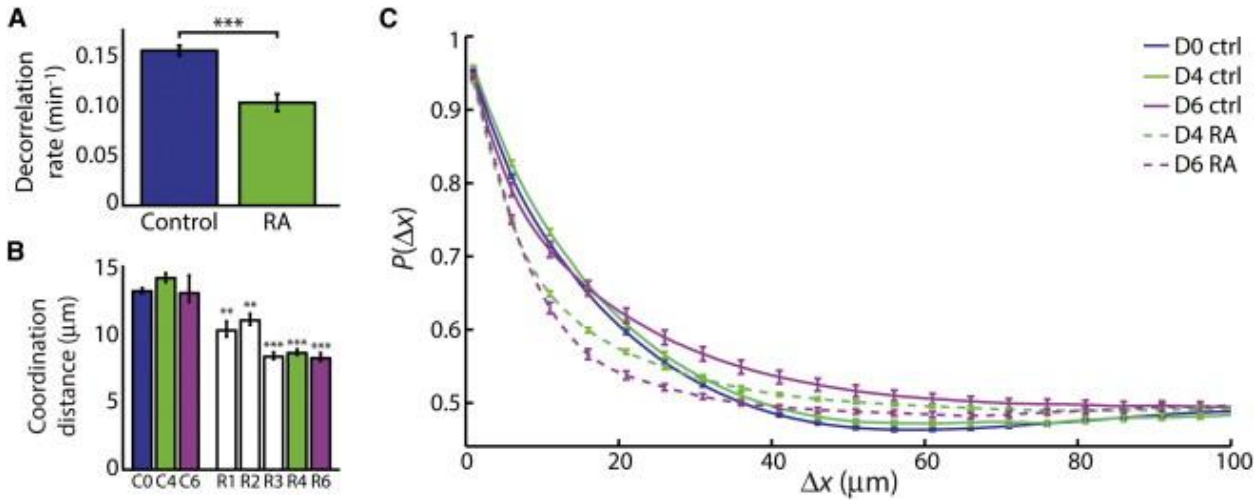

Figure 4-7. Quantification of mass redistribution rate and coordination within hPSC colonies. (**A**) Average decorrelation rates for untreated and RA-treated hPSCs reveals that pluripotent colonies redistribute mass significantly faster than RA-differentiated colonies. (**B**) Coordination distance within a colony is significantly lower in RA-differentiated colonies relative to untreated controls. (**C**) Probability of agreement in mass increase or decrease as a function of displacement (Δx) as measured in 435 untreated colonies 24 h after plating (d 0), 351 RA-treated and 131 untreated colonies on d 4, and 75 RA-treated and 88 untreated colonies on d 6 of RA treatment. For clarity, error bars are only shown on every 5th point. Error bars show +/- SE ** $p < 0.001$, *** $p < 10^{-5}$.

Supplementary Information

Movies S1- S4. Movies illustrating colony motion and LCI time-lapse measurements of mass distributions. **Movies S1** and **S2** each show one untreated (control) colony for 110 and 45 minutes, respectively. **Movie S3** shows a colony from day 4 of retinoic acid treatment over a period of 80 minutes. **Movie S4** shows a colony from day 6 retinoic acid treatment over a period of 50 minutes.

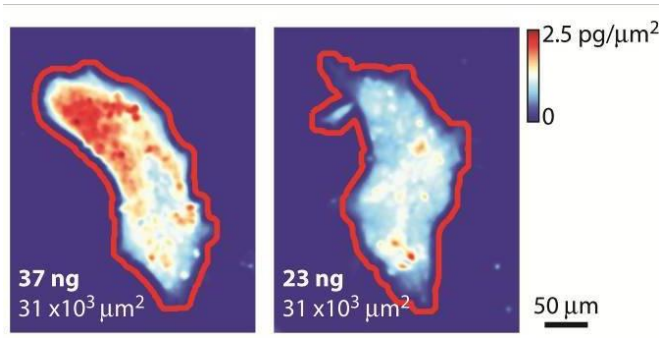

Figure 4-S1. The LCI can determine mass differences in transparent objects of identical area, demonstrating the need for quantitative mass measurements to determine accurate sizes for hPSC colonies. Red outline shows the automatically detected border for these two HSF1 colonies of identical area but unequal mass. In all hPSC measurements, mass is quantified by adding the mass at each imaging pixel within red borders.

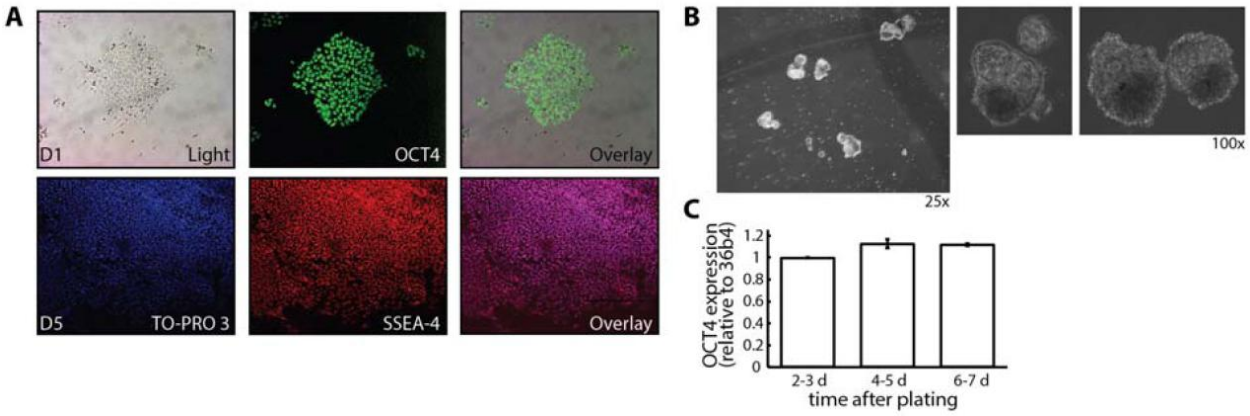

Figure 4-S2. (**A**) Colony morphology of hESCs (HSF1) grown on MEF feeder free Matrigel plate. OCT4 and SSEA-4 staining with immunofluorescence indicates their pluripotency. TO-PRO3 is a nuclear stain to show colocalization of SSEA-4 staining. (**B**) Embyoid bodies formed from hESC line HSF1 used in this study. The three-dimensional spheroid aggregates of differentiated pluripotent cells were cultured in EB media for ~10 d, and resembled early embryonic germ-layer development. The outer layer of cells represent differentiated trophoectoderm and the darker region in the embryoid body represent formation of embryonic cavity. EBs have the potential to differentiate into three, typically disorganized, germ layers. (**C**) OCT4 gene expression data over 6-7 days in culture shows maintenance of pluripotency. Error bars show SE.

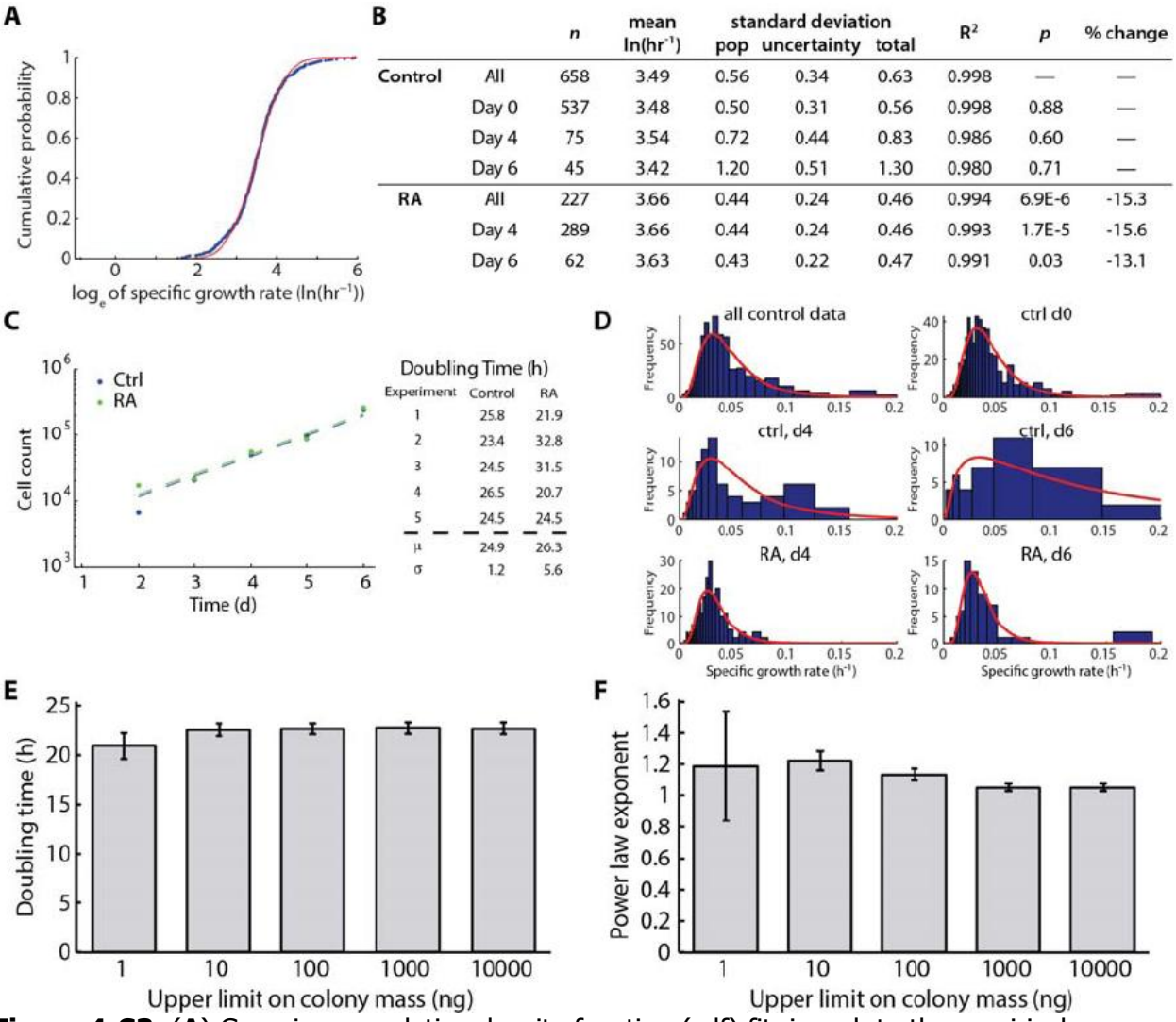

		n	mean ln(hr^{-1})	standard deviation pop	uncertainty	total	R^2	p	% change
Control	All	658	3.49	0.56	0.34	0.63	0.998	—	—
	Day 0	537	3.48	0.50	0.31	0.56	0.998	0.88	—
	Day 4	75	3.54	0.72	0.44	0.83	0.986	0.60	—
	Day 6	45	3.42	1.20	0.51	1.30	0.980	0.71	—
RA	All	227	3.66	0.44	0.24	0.46	0.994	6.9E-6	-15.3
	Day 4	289	3.66	0.44	0.24	0.46	0.993	1.7E-5	-15.6
	Day 6	62	3.63	0.43	0.22	0.47	0.991	0.03	-13.1

Figure 4-S3. (**A**) Gaussian cumulative density function (cdf) fit, in red, to the empirical cumulative probability, in blue, demonstrating the method used to estimate the mean and standard deviation of specific growth rate. Data shown is for all control colonies. (**B**) Summary of results for cdf fitting and Monte Carlo routine incorporating uncertainty in measured colony growth rates. n is number of colonies in each category. Mean and standard deviation are presented as the mean of the logarithm base e of the specific growth rate (hr^{-1}). Standard deviations are presented for: the population without uncertainty, the distribution of means due to consideration of uncertainty in growth rate (this is the standard deviation of all sample means from the Monte Carlo analysis), the total standard deviation (due to both underlying

population standard deviation and uncertainty in growth rate, calculated as the average standard deviation from all cdf curve fits in the Monte Carlo analysis). R^2 quantifies goodness of fit for the cdf fit to the population data (as in A). p values and percent change are calculated relative to all control data. (**C**) Sample cell counting data used to estimate proliferation rate with linear best fit line (on logarithmic scale) used to calculate doubling rate and all doubling times as determined in each cell counting experiment. (**D**) Lognormal curve fits for individual measurement days, as in Figure 3B. (**E, F**) Performing the specific growth rate analysis (E) or power law scaling analysis (F) for restricted ranges of colony size has little effect on the final result. Error bars show s.d.

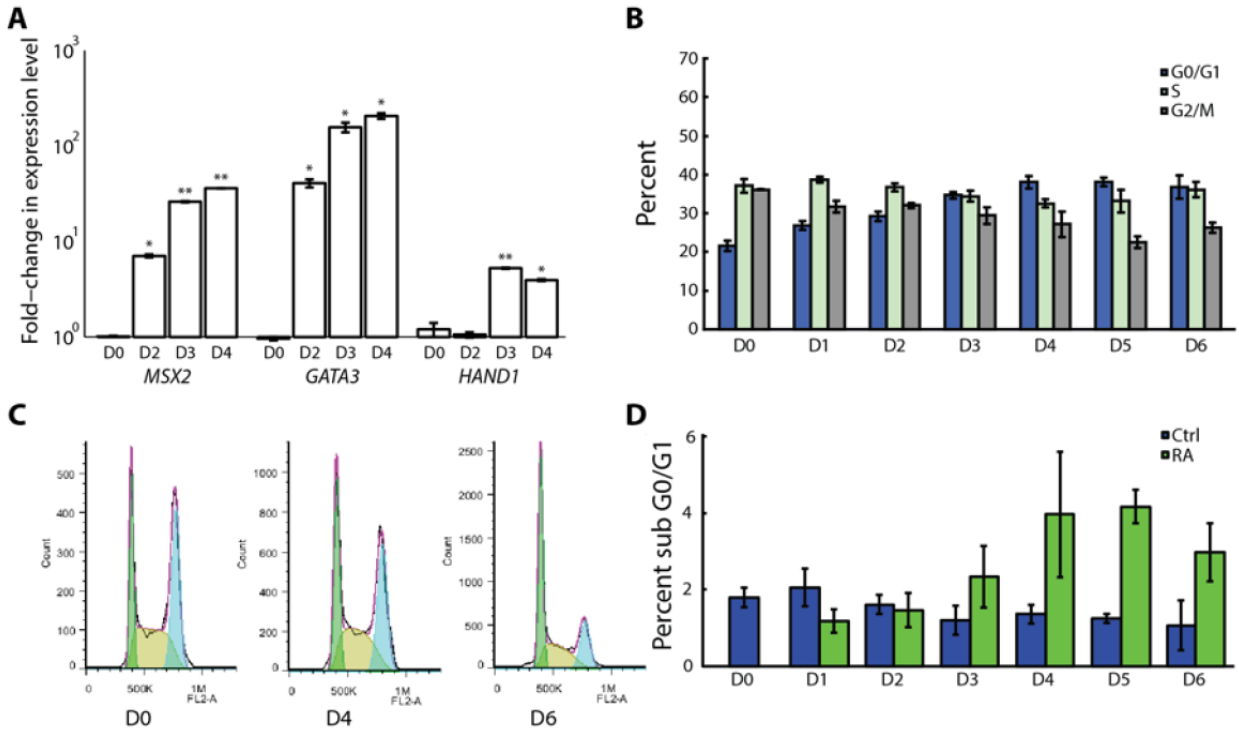

Figure 4-S4. (**A**) changes in hPSC expression of MSX2, GATA3 and HAND1 trilineage differentiation genes after 0, 2, 3 and 4 d of RA exposure. (**B**) Cell cycle analysis of cells from control colonies on successive days of the experiment. (**C**) Representative YOYO-1 fluorescence intensity curve fits for RA-treated cells at 0, 4 and 6 d. (**D**) Percent sub-G0/G1 cells over 6 days of RA treatment. Error bars show SE, *p<0.05, **p<0.01 relative to control data.

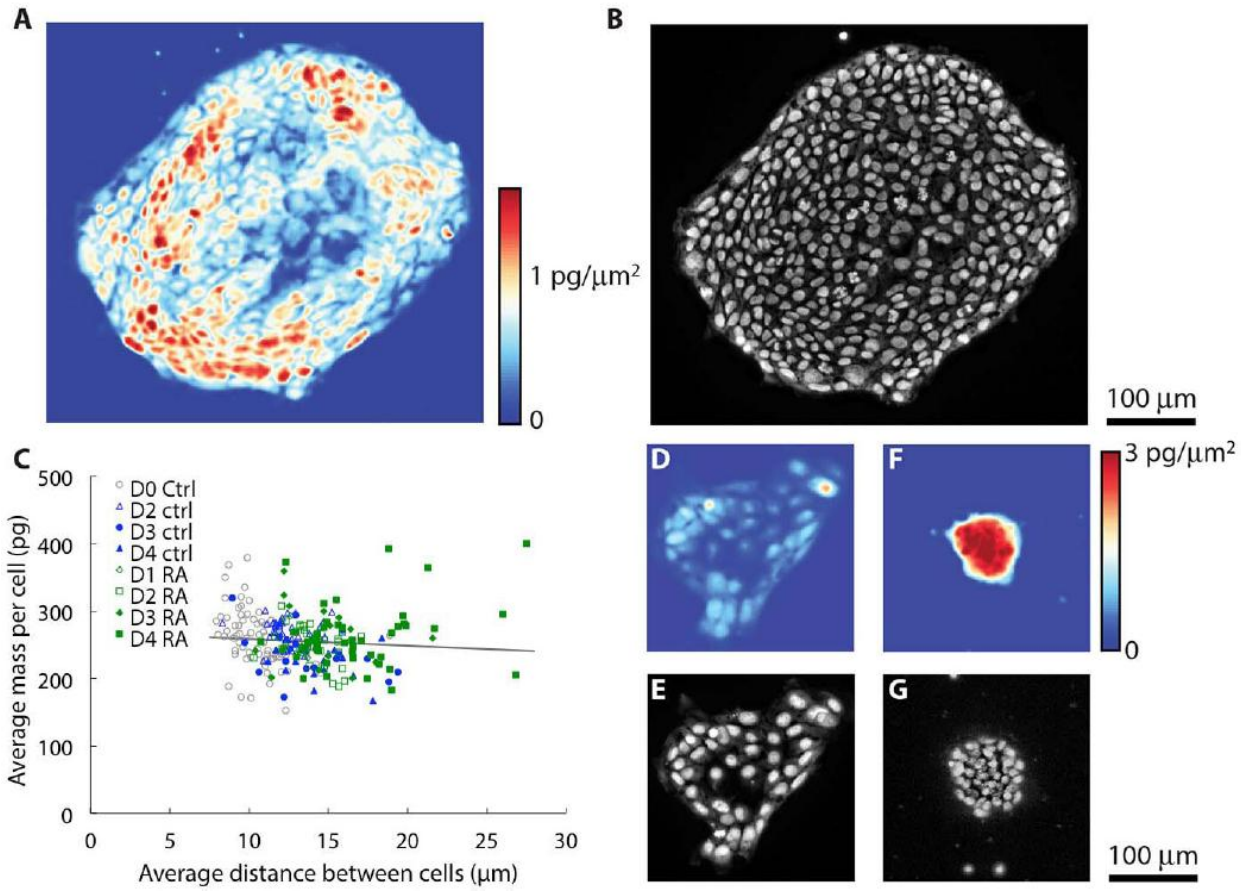

Figure 4-S5. Phase and fluorescence measurements illustrating single cell mass measurement for sample colonies and average mass per cell as a function of the distance between cells. (**A**) Quantitative phase image of a colony from d 4 of RA treatment with a total mass of 90.6 ng. (**B**) The corresponding fluorescence image of YOYO-1 stained nuclei gives a count of 392 cells. Together this yields 231 pg as the estimated average mass per cell. (**C**) Average mass per cell plotted against the average distance between cells with least squares best fit line shown in dark grey. The average distance between cells increases as colonies take on a more differentiated appearance. The slope of this line is not statistically significant from zero, indicating that there is no evidence for a relationship between these two parameters, further supporting the conclusion that cell mass is unchanged during early differentiation. (**D, E**) Phase and fluorescence images of sample RA-treated colony (day 4 of treatment) with an average distance

between cells of 19.9 μm and an average mass per cell of 277 pg. (**F, G**) Phase and fluorescence images of sample control, untreated colony (24 hours after plating) with an average distance between cells of 10.1 μm and an average mass per cell of 232 pg.

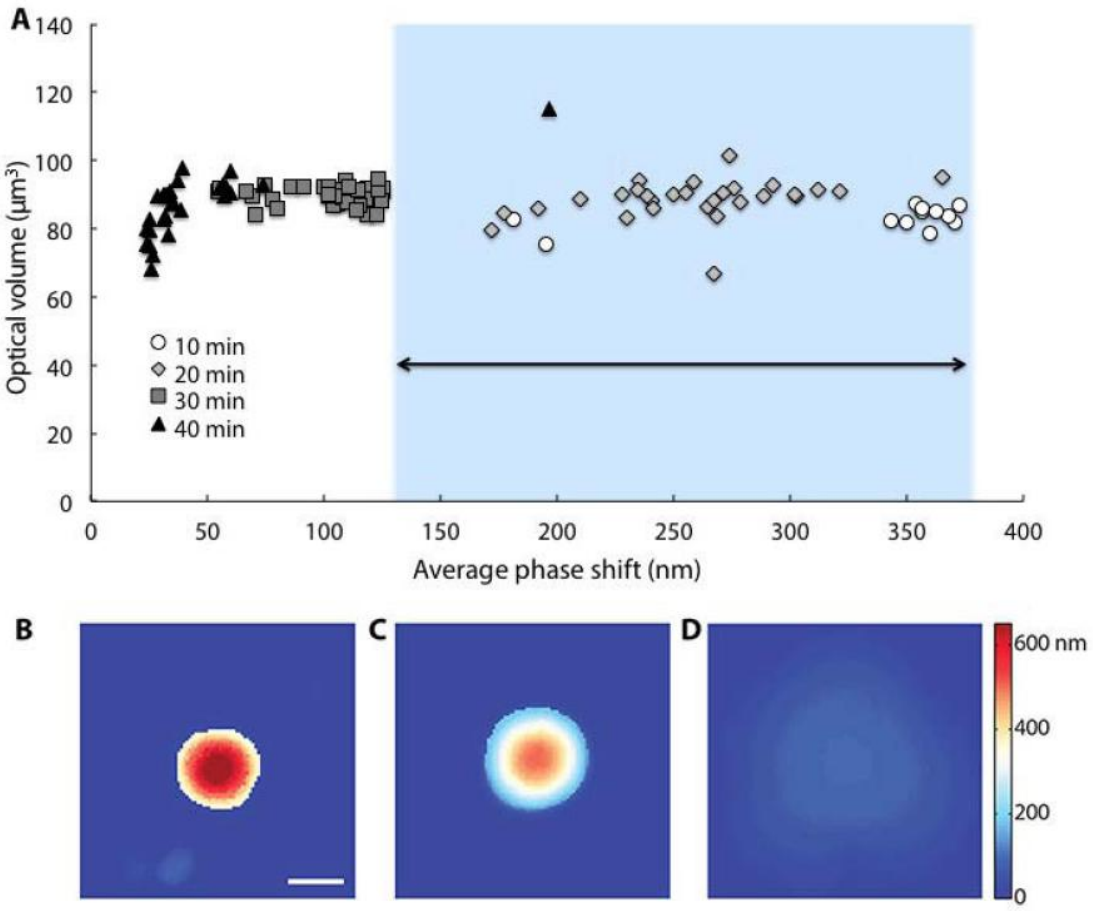

Figure 4-S6. Calibration measurements of polystyrene beads melted onto a silicon substrate for the indicated amount of time to generate calibration standards of uniform optical volume, with variable average phase shift from very flat beads (low average phase shift) to very high, round beads (high phase shift). (**A**) Typical stem cell colony measurement range indicated in blue, showing that LCI measurements of stem cell mass are insensitive to changes in cell morphology shift over the range of measured phase shifts. (**B**)-(**D**) images of polystyrene beads melted for 10 (B), 20 (C), and 40 (D) minutes with average phase shifts of 372, 240, and 60 nm, respectively. These melted beads all have measured optical volumes equal to the overall mean +/- 2.6%. Scale bar in (B) is 10 μm.

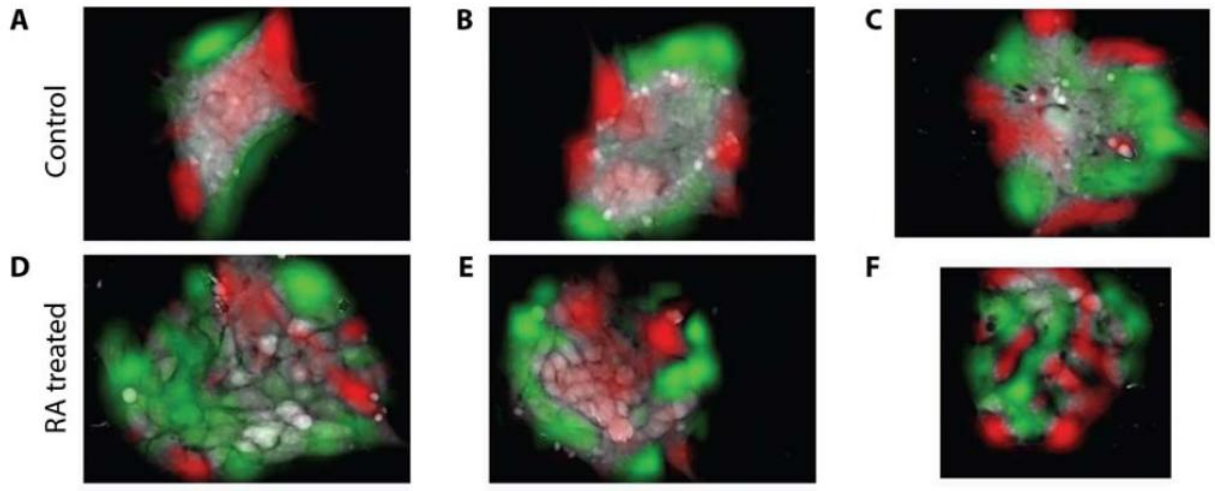

Figure 4-S7. Additional local mass accumulation plots, as in Figure 6A and D. Top row shows control colonies. Bottom row shows RA-treated colonies.

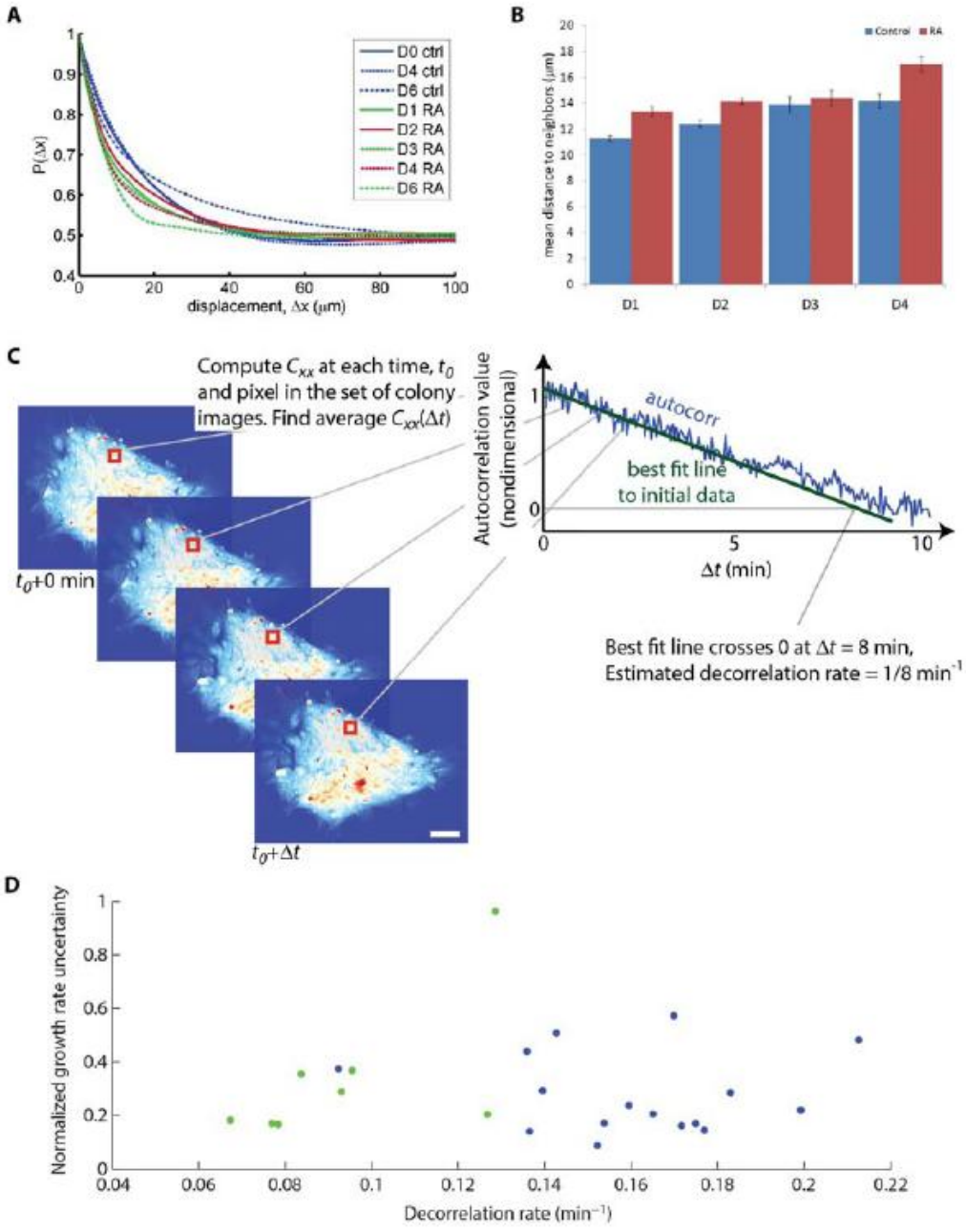

Figure 4-S8. (**A**) P(Δx) vs. displacement for all RA colonies, including those measured after 1-3 d of RA treatment showing the gradual loss of coordination during the first two days of RA treatment. n = 62, 121 and 106 for 1, 2 and 3 d of RA treatment. (**B**) Average distance between cells for control and RA-treated colonies, based on distance between nuclei centers from fluorescence images. (**C**) Illustration of decorrelation timescale. Average autocorrelation,

C_{xx},is computed across all pixel locations within the image stack. Then a linear best fit line is applied to the initial 5 minutes of $C_{xx}(\Delta t)$. Δt at the zero crossing of this line defines the decorrelation timescale. The inverse of this timescale is the decorrelation rate. Error bars show SE. (**D**) normalized uncertainty in growth rate measurement (calculated as the standard deviation of the growth rate estimate) plotted against the decorrelation rate. Intracolony motion shows no effect on the uncertainty in growth rate.

Supplementary Analysis: Theoretical growth rate vs. mass for large colonies

In this section we will show that the observed linear relationship between colony mass accumulation and growth rate is expected regardless of the mass vs. time relationship of individual cells within the colony. Consider the total mass, *M*, of a colony composed of *n* individual cells, m_i, given by:

$$M = \sum_{i=1}^{n} m_i \ .$$

First, we will look at the relationship between the mass accumulation rate of the colony and the masses of the individual cells which comprise that colony. Differentiation in time yields the rate of mass accumulation of the colony in terms of the mass accumulation rate of each of its constituent cells:

$$\frac{dM}{dt} = \sum_{i=1}^{n} \frac{dm_i}{dt} \ .$$

If we assume that *n* is large, and that the cells in the colony are not cell-cycle synchronized (which is consistent with our observation that only a small, consistent fraction of cells within large colonies stained for DNA are mitotic), then we can write:

$$\frac{dM}{dt} \approx n\overline{\frac{dm}{dt}} \ ,$$

where $\overline{dm/dt}$ is the average mass accumulation rate of an individual cell across the cell cycle. If we assume that each individual cell starts at an initial mass, m_0, and divides when it reaches twice this size, then we can write:

$$\overline{\frac{dm}{dt}} = \frac{1}{t_{cycle}} \int_0^{t_{cycle}} \frac{dm}{dt}(t)\,dt = \left[m\right]_0^{t_{cycle}} = \frac{m_0}{t_{cycle}} \ .$$

Therefore:

$$\frac{dM}{dt} = n\frac{m_0}{t_{cycle}}.$$

Now we will consider the relationship of the colony total mass to the mass of its constituent cells. Given the same assumptions above, for the total mass of the colony, we can write:

$$M \approx n \cdot \overline{m},$$

where $\overline{m}$ is the cell-cycle averaged mass of the cells within the colony:

$$\overline{m} = \frac{1}{t_{cycle}} \int_0^{t_{cycle}} m(t)\, dt.$$

Before we consider the general case, first, consider the case of purely exponential mass accumulation, $m = m_0 e^{t/\tau}$, where m is the mass of an individual cell, m_0 is the mass of this cell at division, t is time, and τ is the exponential time constant for mass accumulation ($\tau = \ln(2) = t_d$, where t_d is the doubling time for mass). In this case:

$$\overline{m} = \frac{m_0}{t_{cycle}} \tau \left(e^{t_{cycle}/\tau} - 1 \right).$$

Recognizing that $2m_0 = m_0 e^{t_{cycle}/\tau}$:

$$\overline{m} = \frac{m_0}{t_{cycle}} \tau.$$

Plugging this into our relationship for total colony mass, and combining with the relationship for colony average mass yields:

$$M = n\frac{m_0}{t_{cycle}} \tau = \tau \frac{dM}{dt}.$$

Therefore, if the cell cycle parameters stay constant with increasing colony size, the expected colony mass accumulation rate is directly proportional to the total mass of the colony.

Next, if we consider the general case where *m* is continuous and lies on the interval $\left[m_0, 2m_0\right]$ over the duration of a cell cycle of duration t_{cycle}, with $t \in \left[0, t_{cycle}\right]$, by the mean value theorem we can write:

$$\overline{m} = \frac{1}{t_{cycle}} \int_0^{t_{cycle}} m(t)\,dt = \frac{m(c)}{t_{cycle}},$$

where $c \in \left[0, t_{cycle}\right]$, therefore the average mass, $\overline{m}$, is equal to some value on the interval $\left[m_0, 2m_0\right]$. This means, for any mass vs. time relationship, we can find a number, *k*, such that:

$$\overline{m} = k \cdot \frac{m_0}{t_{cycle}}.$$

Therefore, we can write:

$$M = n \cdot k \cdot \frac{m_0}{t_{cycle}} = k \frac{dM}{dt}.$$

Again, the colony mass accumulation rate is directly, linearly proportional to the total mass of the colony, as long as the parameter *k* is independent of colony size. If *k* were dependent on colony size, we would expect a the relationship between *M* and *dM* / *dt* to be described by a super- or sub-linear, powerlaw relationship. Therefore, to test this model prediction, we perform nonlinear least squares fitting to a powerlaw, $M = k\left(dM/dt\right)^p$, where *p* is the scaling exponent. Also, note that the constant of proportionality, *k*, can be easily computed for any other assumed mass accumulation profile. For example, in the exponential case above, *k* = ·, or in the case of constant, linear growth, $m = m_0\left(t / t_{cycle} + 1\right)$, $k = \frac{3}{2} t_{cycle}$.

References

1. Kim, J., J. Chu, X. Shen, J. Wang, and S. H. Orkin. 2008. An extended transcriptional network for pluripotency of embryonic stem cells. Cell 132:1049-1061.

2. Takahashi, K., and S. Yamanaka. 2006. Induction of pluripotent stem cells from mouse embryonic and adult fibroblast cultures by defined factors. Cell 126:663-676.

3. Smith, Z. D., I. Nachman, A. Regev, and A. Meissner. 2010. Dynamic single-cell imaging of direct reprogramming reveals an early specifying event. Nat Biotechnol 28:521-526.

4. Loh, K. M., and B. Lim. 2010. Recreating pluripotency? Cell Stem Cell 7:137-139.

5. Singh, A. M., and S. Dalton. 2009. The cell cycle and Myc intersect with mechanisms that regulate pluripotency and reprogramming. Cell Stem Cell 5:141-149.

6. Li, L., B. H. Wang, S. Wang, L. Moalim-Nour, K. Mohib, D. Lohnes, and L. Wang. 2010. Individual cell movement, asymmetric colony expansion, rho-associated kinase, and E-cadherin impact the clonogenicity of human embryonic stem cells. Biophys J 98:2442-2451.

7. Keller, P. J., A. D. Schmidt, J. Wittbrodt, and E. H. Stelzer. 2008. Reconstruction of zebrafish early embryonic development by scanned light sheet microscopy. Science 322:1065-1069.

8. Lawson, K. A., J. J. Meneses, and R. A. Pedersen. 1991. Clonal analysis of epiblast fate during germ layer formation in the mouse embryo. Development 113:891-911.

9. Tzur, A., J. K. Moore, P. Jorgensen, H. M. Shapiro, and M. W. Kirschner. 2011. Optimizing optical flow cytometry for cell volume-based sorting and analysis. PLoS One 6:e16053.

10. Godin, M., F. F. Delgado, S. Son, W. H. Grover, A. K. Bryan, A. Tzur, P. Jorgensen, K. Payer, A. D. Grossman, M. W. Kirschner, and S. R. Manalis. 2010. Using buoyant mass to measure the growth of single cells. Nat Methods 7:387-390.

11. Park, K., L. J. Millet, N. Kim, H. Li, X. Jin, G. Popescu, N. R. Aluru, K. J. Hsia, and R. Bashir. 2010. Measurement of adherent cell mass and growth. Proc Natl Acad Sci U S A 107:20691-20696.

12. Ross, K. F. A. 1967. Phase Contrast and Interference Microscopy for Cell Biologists. St. Martin's Press, New York.

13. Reed, J., J. Chun, T. A. Zangle, S. Kalim, J. S. Hong, S. E. Pefley, X. Zheng, J. K. Gimzewski, and M. A. Teitell. 2011. Rapid, massively parallel single-cell drug response measurements via live cell interferometry. Biophys. J. 101:1025-1031.

14. Mir, M., Z. Wang, Z. Shen, M. Bednarz, R. Bashir, I. Golding, S. G. Prasanth, and G. Popescu. 2011. Optical measurement of cycle-dependent cell growth. Proc. Natl. Acad. Sci. USA

108:13124-13129.

15. Mitchison, J. M. 1957. The growth of single cells: I. Schizosaccharomyces pombe. Exp. Cell Res. 13:244-262.

16. Pavillon, N., J. Kuhn, C. Moratal, P. Jourdain, C. Depeursinge, P. J. Magistretti, and P. Marquet. 2012. Early cell death detection with digital holographic microscopy. PLoS One 7:e30912.

17. Park, Y., C. A. Best, K. Badizadegan, R. R. Dasari, M. S. Feld, T. Kuriabova, M. L. Henle, A. J. Levine, and G. Popescu. 2010. Measurement of red blood cell mechanics during morphological changes. Proc Natl Acad Sci U S A 107:6731-6736.

18. Bon, P., Savatier, J., Merlin, M., Wattellier, B., Monneret, S. 2012. Optical detection and measurement of living cell morphometric features with single-shot quantitative phase microscopy. Journal of Biomedical Optics 17:076004.

19. Anand, A., Chhaniwal, V.K., Javidi, B. 2011. Imaging Embryonic Stem Cell Dynamics Using Quantitative 3-D Digital Holographic Microscopy. Photonics Journal, IEEE 3:546-554.

20. Reed, J., J. J. Troke, J. Schmit, S. Han, M. A. Teitell, and J. K. Gimzewski. 2008. Live Cell Interferometry Reveals Cellular Dynamism During Force Propagation. ACS Nano 2:841-846.

21. Zhang, J., I. Khvorostov, J. S. Hong, Y. Oktay, L. Vergnes, E. Nuebel, P. N. Wahjudi, K. Setoguchi, G. Wang, A. Do, H. J. Jung, J. M. McCaffery, I. J. Kurland, K. Reue, W. N. Lee, C. M. Koehler, and M. A. Teitell. 2011. UCP2 regulates energy metabolism and differentiation potential of human pluripotent stem cells. EMBO J 30:4860-4873.

22. Zhang, J., E. Nuebel, D. R. Wisidagama, K. Setoguchi, J. S. Hong, C. M. Van Horn, S. S. Imam, L. Vergnes, C. S. Malone, C. M. Koehler, and M. A. Teitell. 2012. Measuring energy metabolism in cultured cells, including human pluripotent stem cells and differentiated cells. Nat Protoc 7:1068-1085.

23. Kohen, N. T., L. E. Little, and K. E. Healy. 2009. Characterization of Matrigel interfaces during defined human embryonic stem cell culture. Biointerphases 4:69-79.

24. Ghiglia, D. C., and M. D. Pritt. 1998. Two-Dimensional Phase Unwrapping: Theory, Algorithms, and Software. John Wiley & Sons, New York, NY.

25. Otsu, N. 1979. A Threshold Selection Method from Gray-Level Histograms. Systems, Man and Cybernetics, IEEE Transactions on 9:62-66.

26. Zar, J. H. 2010. Biostatistical Analysis. Pearson Prentice Hall, Upper Saddle River, New Jersey.

27. Bendat, J. S., and A. G. Piersol. 2000. Random Data: Analysis and Measurement Procedures. John Wiley & Sons.

28. Sund, S. E., and D. Axelrod. 2000. Actin dynamics at the living cell submembrane imaged by total internal reflection fluorescence photobleaching. Biophys J 79:1655-1669.

29. Lowry, W. E., L. Richter, R. Yachechko, A. D. Pyle, J. Tchieu, R. Sridharan, A. T. Clark, and K. Plath. 2008. Generation of human induced pluripotent stem cells from dermal fibroblasts. Proc Natl Acad Sci U S A 105:2883-2888.

30. Zhou, W., M. Choi, D. Margineantu, L. Margaretha, J. Hesson, C. Cavanaugh, C. A. Blau, M. S. Horwitz, D. Hockenbery, C. Ware, and H. Ruohola-Baker. 2012. HIF1[alpha] induced switch from bivalent to exclusively glycolytic metabolism during ESC-to-EpiSC/hESC transition. EMBO J. 31:2103-2116.

31. Bryan, A. K., A. Goranov, A. Amon, and S. R. Manalis. 2010. Measurement of mass, density, and volume during the cell cycle of yeast. Proc. Natl. Acad. Sci. USA 107:999-1004.

32. Park, Y., C. A. Best, K. Badizadegan, R. R. Dasari, M. S. Feld, T. Kuriabova, M. L. Henle, A. J. Levine, and G. Popescu. 2010. Measurement of red blood cell mechanics during morphological changes. Proc. Natl. Acad. Sci. USA 107:6731-6736.

CHAPTER 5

Conclusion

The LCI technology enables accurate quantification of the dry mass of hundreds of cells or colonies over time without labels or manipulations of the sample culture. As we have demonstrated, the interferometric method is repeatable on a wide range of cell-shaped bodies and stable for longitudinal studies. We have shown mass dynamics of drug responses in cancer cell lines and differentiating human pluripotent stem cells. Furthermore, we have measured shifting mass distributions in stem cell colonies as an indicator of intra-colony motion, which replicates cell motion during early embryo patterning events. While these studies have been first trials in a developing technology platform, we have shown the ability of the LCI to accommodate a broad range of cell types and growth, from cancer cell lines to pluripotent stem cells, and single cells to multi-cellular colonies, demonstrating the broad accessibility for this open platform technology.

Due to the high sensitivity and rapid data accumulation of the LCI method, assessing mass changes in cells is orders of magnitude faster than traditional proliferation assays. In addition to increased speed, the single cell nature of the measurements means that it is possible to examine the degree of cellular heterogeneity in the mass response to a stimulus within a population of cells. This individualization not only allows a more detailed, kinetic examination of cell growth and division, it could also provide a potentially superior way to judge the efficacy of drugs in diseases such as cancer where some cells may respond to treatment more readily than others.

While a number of modifications to simplify the LCI operation would be useful in considering its practical use, these improvements are built upon the core technology that has been demonstrated here. Enclosing the entire device in an incubator-based environmentally controllable system would shorten the preparation time for cell sample examinations and reduce extraneous hardware currently in place to maintain a stable environment. Integration of fluorescence light sources and objectives would also allow easier interchangeability between imaging modes to more conveniently monitor cell signaling almost simultaneously along with changes in dry cell mass over time. Including an optional longer wavelength light source would be useful as well for samples that are more optically dense or overlapping.

In addition to revealing new information on cell growth and division, further development of the live cell interferometer and the associated sample preparation procedures could yield more individualized cancer treatments. The speed of the drug efficacy assessment by the LCI could enable a panel of therapies to be tested on a patient sample to help choose the best treatment for that individual. This type of direct assessment would be a valuable advancement in cancer treatment.